Effect of Screening Currents on the Field Quality of HTS Pancake Coil Magnets

Master's Thesis of

Marco Moretti

at the
Institute for Institute for Technical Physics (ITEP)

Reviewer:	Prof. Francesco Grilli
Second reviewer:	Prof. Roberto Bonifetto
Advisor:	Dr. Asef Ghabeli

15. April 2025 – 15. October 2025

Politecnico di Torino
Dipartimento Energia “Galileo Ferraris”
Corso Duca degli Abruzzi 24
10129 Torino – Italy

Karlsruher Institut für Technologie
Institute of Technical Physics
Campus North
76344 Karlsruhe - Germany

I declare that I have developed and written the enclosed thesis completely by myself, and have not used sources or means without declaration in the text.

PLACE, DATE

. . . . . .

(Marco Moretti)

Abstract

High-temperature superconductors (HTS) have attracted increasing attention for their ability to carry very high current densities at relatively high temperatures, enabling the development of compact magnets capable of generating strong magnetic fields. These materials are of particular interest for applications in fusion reactors.

This thesis focuses on the electromagnetic behavior of HTS pancake coils, investigated through numerical simulations to analyze how the geometric configuration and the current distribution affect coil performance. The study specifically examines the phenomenon of screening currents, their influence on the central magnetic field, and the dependence of the maximum injectable current on coil geometry. The modeled geometry is comparable in scale to the superconducting components of gyrotrons, although the results obtained have more general relevance.

Three configurations were analyzed: a single pancake, a stack of four pancakes, and a complete ten-pancake coil. The simulations considered different current ramp profiles to evaluate screening current induced fields (SCIF), field relaxation (drift), and the resulting magnetic field quality.

The results show that increasing the number of pancakes amplifies the deviation from the ideal current distribution and reduces the maximum injectable current. Screening current effects become more pronounced as the stack grows, leading to partial current penetration and magnetic field non-uniformities, particularly in the central region of the coil. The most effective mitigation strategies are the inclusion of a central double pancake or the injection of higher current in the central pancakes, improving field uniformity and overall performance.

Contents

List of Figures

List of Tables

1 Introduction

Superconductors have numerous well-documented applications in the nuclear field, particularly in nuclear magnetic resonance (NMR), magnetic resonance imaging (MRI), particle accelerators, and both nuclear fission and fusion reactors.

In this thesis, the focus is placed on the use of superconductors for the generation of intense magnetic fields. Numerical simulations of superconducting coils are a powerful tool for the design and optimization of electromagnetic devices, as they allow the analysis of current distribution, magnetic field quality, and critical current limitations under realistic operating conditions.

The first part of this work aims to provide the reader with the theoretical and methodological background necessary to understand the logic behind the simulations. It begins with a concise introduction to the fundamental concepts of superconductivity, followed by a discussion of the role and applications of superconductors in the nuclear field, with particular emphasis on their implementation in nuclear fusion reactors.
Subsequently, the numerical formulations employed for the simulations are presented, and finally, the results obtained from the analysis are discussed and interpreted.

This investigation examines how the number of pancakes affects the electromagnetic behavior of the coil. In particular, the analysis focuses on a ten-pancake configuration, assessing the impact of various current ramp profiles and the effects of Screening current induced field (SCIF), relaxation (field drift) and geometric characteristics on the central magnetic field.

1.1 Fundamentals of Superconductors

1.1.1 Introduction to Superconductivity

The discovery of superconductivity represents a major scientific and technological breakthrough. The term superconductivity refers to a physical phenomenon first observed in 1911 by Heike Kamerlingh Onnes and his assistant Gilles Holst, who recorded the complete disappearance of electrical resistivity in a mercury wire when its temperature was lowered below approximately 4 K. [5]
Later on, researchers demonstrated that a variety of materials — ranging from metals to ceramics — exhibit a drastic reduction in electrical resistance when cooled below a specific temperature, known as the critical temperature (Tc), eventually reaching values that are practically zero. Throughout the 20th century, numerous scientists — several of

whom were awarded the Nobel Prize — contributed to the understanding of the physical mechanisms underlying superconductivity. Their work significantly advanced the global knowledge in the field and laid the foundation for the technological and engineering exploitation of superconducting materials.

Different theories have been formulated over the years to explain this phenomenon. At present, the two main theoretical frameworks that best describe superconductivity are:

- **BCS theory (1957)** — developed by Bardeen, Cooper, and Schrieffer — which explains superconductivity at the microscopic level through the formation of *Cooper pairs*, resulting from electron–phonon interactions.
- **Ginzburg–Landau theory (1950)** — a phenomenological model that describes the macroscopic behavior of superconductors and introduces key parameters such as the coherence length and the magnetic penetration depth.

Key critical parameters

Three parameters defines the limits of the superconductor's region (fig. 1.1):

- Critical Temperature (T_c).
- Critical current density (J_c).
- Critical magnetic field (H_c).

These three parameters — Tc, Jc and Hc — are fundamental for determining the operational limits of superconducting devices. In practical applications, such as magnet design, the interplay between temperature, current, and magnetic field defines the safe operating range of the superconductor. Exceeding any of these limits can cause a transition to the normal resistive state, potentially leading to energy losses or even damage to the coil.

Classification of superconductors

Based on their behavior under applied magnetic fields, superconductors are commonly classified into two types:

- **Type I**: These were the first superconductors discovered and are characterized by a relatively low critical magnetic field, which also limits their critical current density. Type I superconductors exhibit the *Meissner effect*, meaning that magnetic field lines are completely expelled from the bulk of the material when it is in the superconducting state.
- **Type II**: In these materials, magnetic flux penetrates the superconductor in the form of quantized vortices, which are pinned by material defects. This leads to the so-called mixed state, allowing the material to maintain superconductivity even under higher magnetic fields. Type II superconductors are characterized by two critical magnetic fields, H_{c1} and H_{c2}: below H_{c1}, the material behaves like a Type I

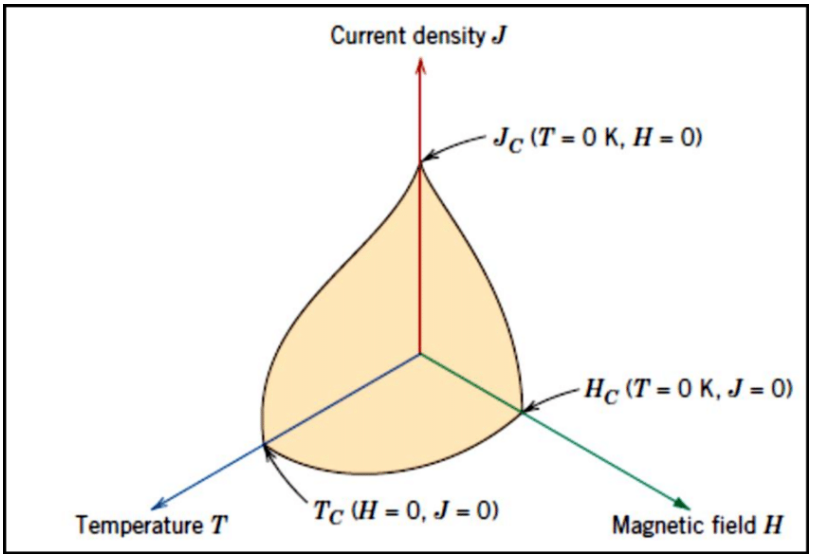

Figure 1.1: The superconducting critical surface, defining the safe operating region for a superconductor in the three-dimensional space of critical current density (J_c), temperature (T), and magnetic field (H)2. (from [10]).

superconductor (*Meissner effect*), while between H_{c1} and H_{c2}, it is in the mixed state, supporting superconductivity under partial flux penetration (see fig 1.2).

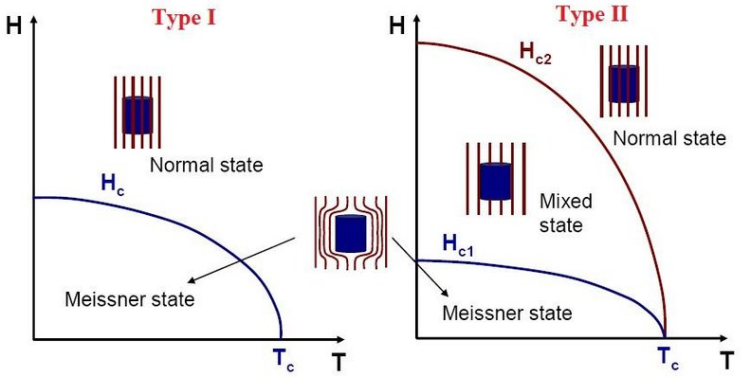

Figure 1.2: Qualitative phase diagram illustrating the behavior of Type I and Type II superconductors under varying temperature (T) and magnetic field (H). Note the mixed state of Type II superconductors existing between H_{c1} and H_{c2}(from [3]).

Research efforts have led to the development of materials with higher critical temperatures, based on various alloys. The most relevant of these materials are shown in Figure 1.3, indicating their critical temperatures and the years in which they were discovered.

A particular class of superconducting materials is the so-called High-Temperature Superconductors (HTS). A common feature of HTS is the presence of copper-oxide layers within their crystalline structure. These materials exhibit higher critical temperatures

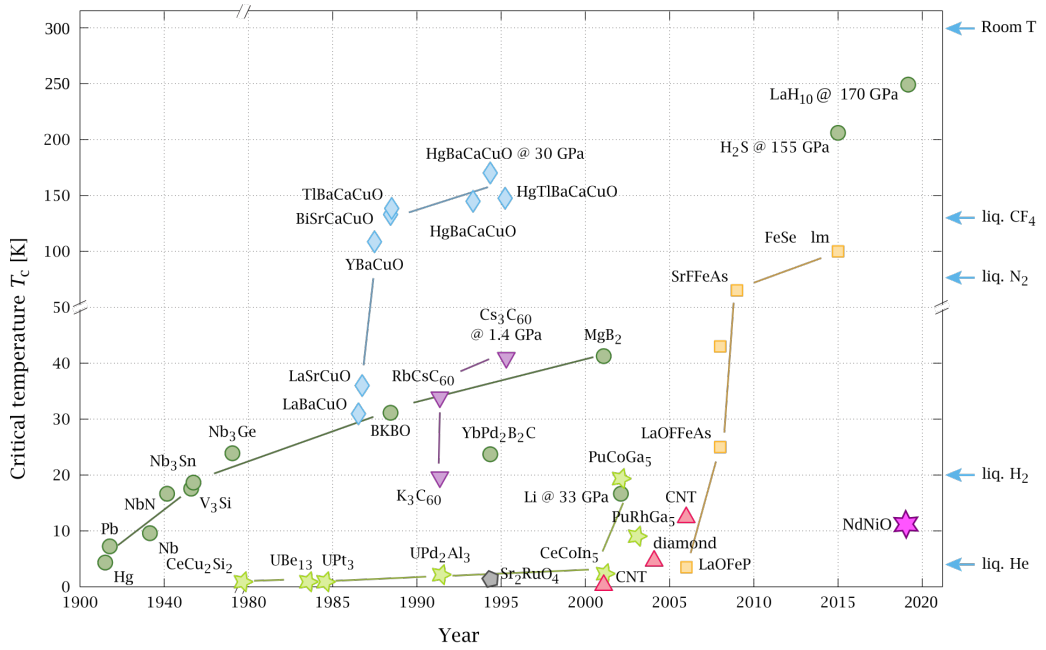

Figure 1.3: Historical timeline of critical temperature (T_c) discoveries in superconducting materials, spanning from 1900 to 2020 (from [11]).

compared to Low-Temperature Superconductors (LTS); however, their layered structure leads to anisotropic behavior, which will be discussed later.

All simulations presented in this thesis focus on this class of materials, which have become increasingly relevant over the last decades relative to LTS.

The first generation of HTS is based on bismuth compounds; for example, $Bi_2Sr_2Ca_2Cu_3O_{10}$ (commonly referred to as Bi-2223 or BSCCO wires). The second generation is based on rare-earth compounds, giving rise to the so-called REBCO tapes and YBCO tapes.

1.1.2 Type II superconductor: flux pinning and vortex dynamics

From a microscopic point of view, type-II superconductors are characterized by a ratio κ between the *penetration depth* λ — the distance over which the magnetic field can vary — and the *coherence length* ξ — the distance over which the density of superconducting electrons (n_s) can vary — that is greater than the critical value $\kappa_c = 1/\sqrt{2}$.

A peculiarity of the Type-II superconductors is the presence of the so-called *vortex regions*, where the magnetic flux penetrates the material in the form of quantized vortices with cylindrical symmetry (fig. 1.5). In this type of superconductors, the electric current is carried through the regions of the sample penetrated by these vortices. The critical current density, in this case, corresponds to the value of J that leads to the *unpinning* of the vortices: this process results in the displacement of the vortex cores, mechanical work being performed, and consequent energy dissipation. [8]

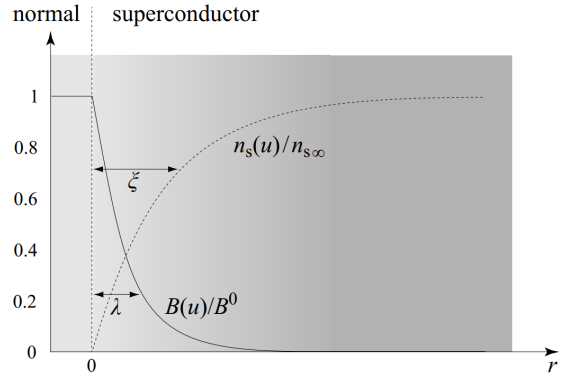

Figure 1.4: Schematic representing the spatial variation of the magnetic field (B) and the density of superconducting electrons (n_s) near a normal/superconducting interface, illustrating the definitions of the magnetic penetration depth (λ) and the coherence length (ξ) (from [8]).

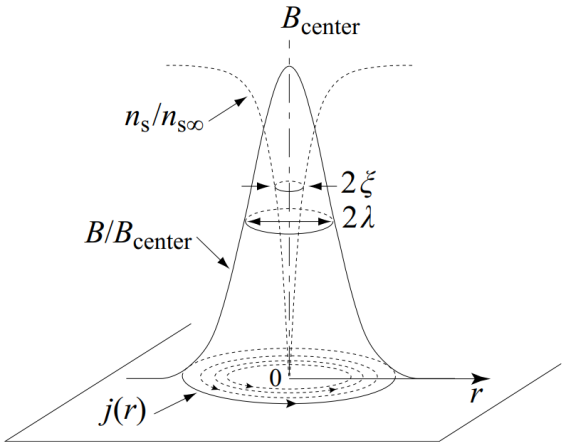

Figure 1.5: Schematic representation of a **vortex**. Starting from the vortex axis, the magnetic field B reaches its maximum B_{center} and decays over the penetration depth λ, while the superconducting electron density increases from zero to its bulk value within the coherence length ξ. Near the vortex core, the magnetic field remains nearly constant due to the low density of London currents (from [8]).

Critical state model

Critical state models (also know as *Bean's Model*) require that at equilibrium, at each point of the superconductor, the current density J must either be equal to the critical current density Jc, or be zero.

$$\text{Critical state} \iff F_\phi = F_p \iff \mathbf{J} = J_c \iff |\nabla \times \mathbf{B}| = \mu_0 J_c.$$

where F_ϕ and F_p denote the Lorentz force and the pinning force, respectively, the latter depending on both the intrinsic properties of the material and its manufacturing process.

The case analyzed in this thesis concerns the simulation of superconducting coils carrying a transport current in the absence of any externally applied magnetic field. The corresponding schematic Bean's model is illustrated in Figure 1.6.

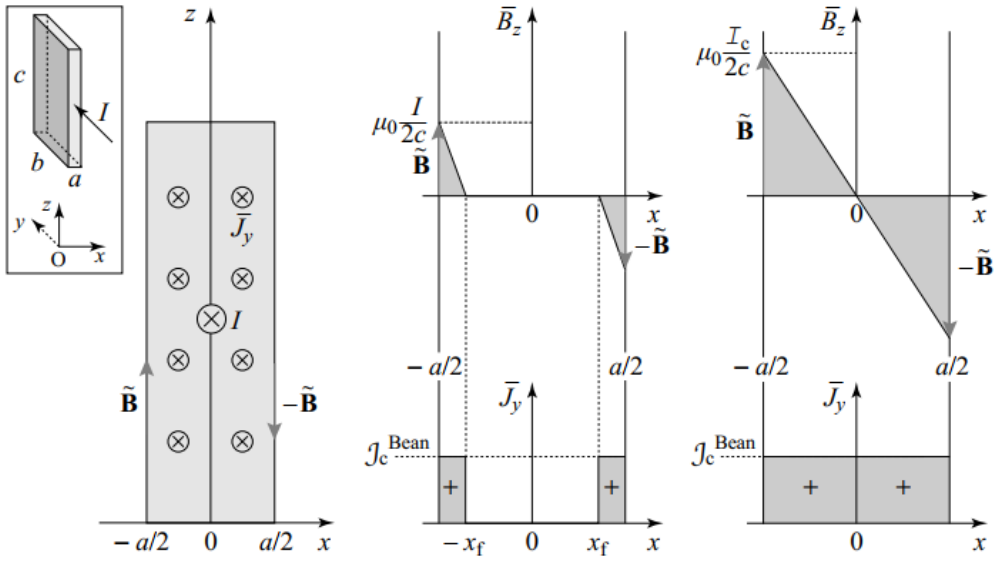

Figure 1.6: Critical states of a superconductor carrying a transport current I in the absence of an external magnetic field (Bean model). The current flows through the cross-section from front to back. For $I < I_c$, the spatial profiles of the magnetic field $B_z(x)$ and current density $J_y(x)$ are shown, while at the critical current $I = I_c$ the superconductor reaches the fully penetrated critical state (from[8]).

Power Law Model

The Power Law Model (*E-J power law*) is a constitutive model that describe the relation between the electric field E and the current density J:

$$E = E_0 \left(\frac{J}{J_c}\right)^n \Leftrightarrow \vec{\mathbf{E}} = E_0 \left(\frac{|\vec{\mathbf{J}}|}{J_c}\right)^{n-1} \frac{\vec{\mathbf{J}}}{J_c} \tag{1.1}$$

Where E_0 is a the threshold value of the electric field (usually chosen equal to 10^{-4}V/m); J_c is the critical density current and n is the power-law index (usually around 30) that represent how sharply is the transition from superconducting state to normal state.

The power law model becomes equal to the critical state model if the pow-law index $n \to \infty$. The chapter 2 will explain how this model is implemented in the mathematical formulation of the numerical model used in the simulations inside the thesis.

1.1.3 Superconducting Coils and HTS magnets

One of the reasons motivating the research carried out in this thesis arises from the intrinsic electromagnetic challenges associated with HTS coils. In conventional resistive coils, the magnetic field distribution can be described directly from Maxwell–Ampère's law, as the current density remains uniform under steady excitation. In contrast, high-temperature superconducting (HTS) coils exhibit a strongly nonlinear electromagnetic behaviour governed by Maxwell's equations coupled with the E–J power law.

The coils investigated in this thesis utilize HTS tapes wound in a configuration where each turn and pancake is electrically insulated from its neighbors. This configuration, often referred to as 'Insulated (I) coils,' ensures that the transport current flows strictly along the path of the tape, maximizing I_c performance but simultaneously enabling the formation of persistent screening currents within the HTS layer itself.

Screening-Currents Induced Field and Field Drift

In HTS coils wound with coated conductor tapes, the large aspect ratio of the tape cross section enhances the formation of screening currents, which are induced by the gradual penetration of the radial magnetic field component during magnetization [13]. Due to the absence of resistive relaxation in the superconducting state, these currents persist after the external excitation, generating a screening current-induced field (SCIF). This contribution not only distorts the overall magnetic field profile but also leads to a temporal field drift even under constant transport current, posing a key challenge for applications requiring high field stability and homogeneity.

The attenuation of the magnetic field caused by Screening currents is expressed by the following relation:

$$B_{SC} = B_{HTS} - B_{id} \tag{1.2}$$

where:

- B_{SC} is the magnetic field contribution due to the screening current;
- B_{HTS} is the magnetic field resulting from the simulation of the HTS coil;
- B_{id} is the magnetic field generated by a uniform current distribution.

In the following chapters, this relation is employed to quantify the *field quality* of the HTS pancake coil.

1.2 Applications and Challenges in HTS Magnets

1.2.1 Nuclear Field Application

One of the most important nuclear applications of superconductors is the generation of magnetic fields for fusion devices. Two key applications in this field will be discussed in the following sections: **Nuclear Fusion Confinement Magnets** and **Gyrotrons**.

Nuclear Fusion Confinement Magnets

The climate crisis and the growing demand for electricity have driven researchers to explore clean energy sources. Nuclear fusion represents the cutting edge of power generation for electricity supply.

The fusion reaction considered in this work is:

$$\mathrm{T}_1^3 + \mathrm{D}_1^2 \longrightarrow \mathrm{He}_2^4 + \mathrm{n}_0^1 + 17.59\ \mathrm{MeV}$$

To achieve a self-sustained fusion reactor, the triple product $nT\tau$ must satisfy *Lawson's criterion*:

$$nT\tau \geq \frac{12T^2}{E_\alpha \langle \sigma v \rangle},$$

where:

- n is the particle density ($n_D = n_T$ for a 50-50 D-T mixture);
- T is the plasma temperature;
- $\tau = \frac{E_{\mathrm{int}}}{P_{\mathrm{loss}}}$ is the confinement time (internal energy over power loss);
- $\langle \sigma v \rangle$ is the velocity-averaged cross section for the fusion reaction;
- E_α is the energy of the helium ion (3.5 MeV).

The minimum temperature and the corresponding triple product are [6]:

$$T_{\mathrm{min}} = 15\,\mathrm{keV} \approx 1.7 \cdot 10^8\,\mathrm{K},$$

$$(n\tau)_{\mathrm{min}} \approx 10^{20}\,\mathrm{s/m^3}.$$

This value does not include any *external heating*, but only the internal heating from alpha particles. Expressed in terms of plasma pressure at $T = 15$ keV:

$$(n\tau)_{\mathrm{min}} \approx 8.4\,\mathrm{MPa \cdot s}.$$

There are two main approaches to achieve these conditions:

- **Inertial Confinement Fusion (ICF)**: operates at extremely high particle density ($n \approx 10^{31}\,\mathrm{m^{-3}}$) and very short confinement time ($\tau \approx 10^{-11}$ s);

- **Magnetic Confinement Fusion (MCF)**: operates with longer confinement times (seconds) and particle density around $n \approx 10^{20}\ \mathrm{m}^{-3}$.

At the required temperatures ($\sim 10^8$ K), the D-T fuel is fully ionized and forms a *plasma*. Magnetic confinement fusion devices exploit the motion of charged particles in magnetic fields (magnetohydrodynamics, MHD) to confine the plasma. Simple toroidal fields are insufficient due to particle drifts [6]; instead, twisted trajectories are required. Two main approaches are used to create these magnetic geometries (see Figure 1.8):

- **Tokamaks**: based on the superposition of three different magnetic fields. Examples include ITER (France), JET (UK), EAST (China), JT-60SA (Japan), K-STAR (Korea), and SPARC (USA).
- **Stellarators**: based on complex coil geometries. Examples include Wendelstein 7-X (Germany) and Stellaris (Proxima Fusion, Germany).

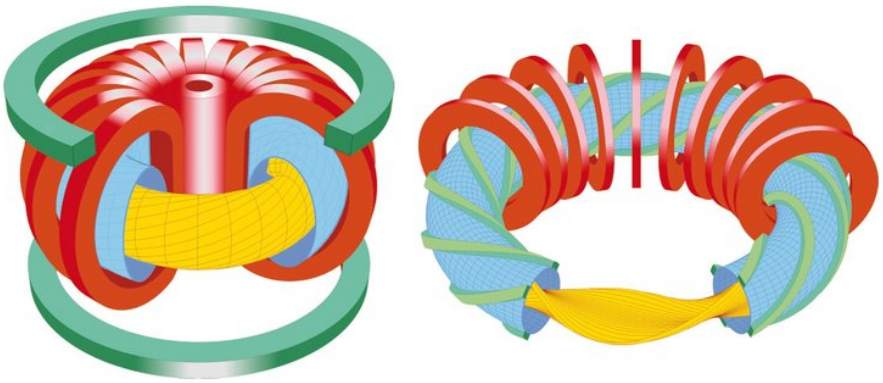

Figure 1.7: Schematic comparison of the two principal Magnetic Confinement Fusion (MCF) device geometries: the Tokamak (left) and the Stellarator (right) (from [10]).

To understand why superconductors are essential for fusion devices, it is useful to consider some basic scaling relations.

First, the fusion power can be related to the reactor size (R) and the magnetic field intensity (B). An important parameter for plasma stability is the *beta* parameter, defined as the ratio between the plasma pressure and the magnetic pressure:

$$\beta = \frac{p}{B^2/2\mu_0}.$$

For stable operation, β must remain below approximately 3–5%. From this, it follows that

$$p \propto B^2 \quad \Rightarrow \quad nT \propto B^2.$$

The fusion power in a magnetic confinement fusion (MCF) device can be expressed as:

$$P_{\text{fus}} \propto n^2 \langle \sigma v \rangle V \quad \Rightarrow \quad P_{\text{fus}} \propto n^2 R^3 \quad \Rightarrow \quad P_{\text{fus}} \propto B^4 R^3.$$

Another key engineering parameter in fusion device is the power gain factor Q, defined as the ratio between the fusion power output and the external heating power. Figure 1.8 shows the relationship between Q, B, R, and the type of material technology used for the magnetic field generation.

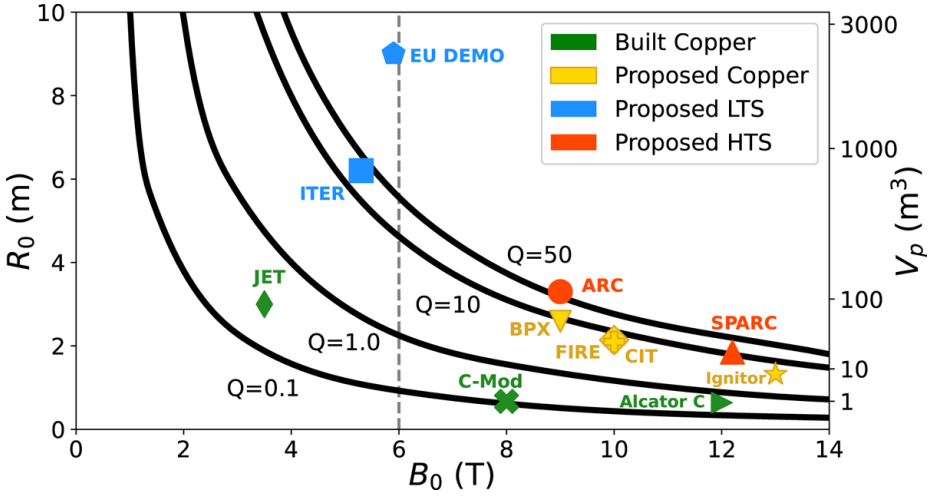

Figure 1.8: Plot showing the Fusion Gain Factor (Q) contours relative to the toroidal magnetic field (B_0) and major radius (R_0), illustrating the technological advantage of High-Temperature Superconductors (HTS) in enabling compact fusion devices (from [4]).

In order to generate the high magnetic fields required for compact fusion reactors, conventional conductors such as copper or aluminum are insufficient due to excessive Joule heating. Superconductors, on the other hand, can sustain large currents without resistive losses, making them the only viable option for producing the multi-tesla fields needed in modern magnetic confinement devices.

Among superconductors, High-Temperature Superconductors (HTS) such as REBCO tapes offer additional advantages. Their higher critical current density and ability to operate at elevated temperatures (compared to low-temperature superconductors) allow the design of more compact and efficient magnets. This capability is particularly important for advanced fusion concepts where strong magnetic fields and precise field quality are required to maintain plasma stability and minimize drift effects.

This research forms part of a dedicated project, commissioned by Proxima Fusion, a European fusion energy company focusing on compact stellarators, to the Karlsruhe Institute of Technology (KIT) – ITEP. The aim of this collaboration is to provide essential modeling for HTS superconducting magnets, which are critical for the design and realization of next-generation fusion devices, such as the Stellarator concept currently pursued by Proxima Fusion.

The focus of this thesis is on the electromagnetic behavior of HTS coils, specifically pancake coil configurations. By simulating these coils, it is possible to predict the maximum

current that can be injected while maintaining superconductivity, analyze the current distribution, and evaluate the resulting magnetic field quality. These simulations provide essential guidance for the design of superconducting magnets in fusion reactors, bridging fundamental superconductivity theory with practical engineering applications.

Gyrotrons

A gyrotron is an electron tube that generates high-frequency, high-power electromagnetic waves, which are essential for Electron Cyclotron Resonance Heating (ECRH) and Electron Cyclotron Current Drive (ECCD) in fusion reactors. ECRH is a mature technology used in magnetic confinement fusion (MCF) to heat the plasma, while ECCD is employed to control plasma stability by providing a tailored current profile.

The key components of a gyrotron are [12]:

- **CVD Diamond Window:** Allows the RF waves to exit the device while maintaining vacuum inside.
- **Single Stage Depressed Collector:** Recovers energy from the spent electron beam, reducing cathode power consumption while maintaining RF output.
- **Superconducting Magnets (SCMs):** Provide the magnetic field that guides the electron beam and determines the operating frequency.

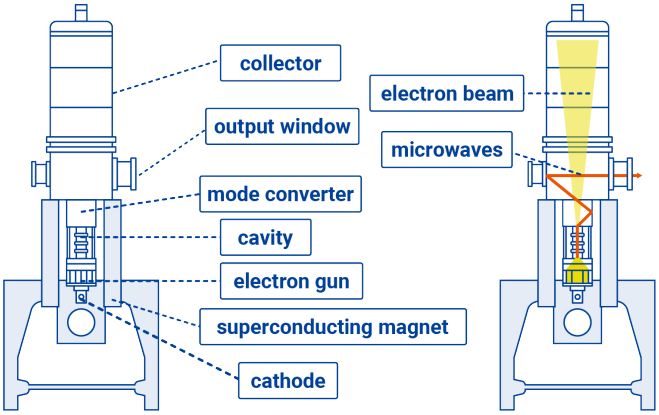

Figure 1.9: Schematic overview of a Gyrotron, highlighting the essential role of the Superconducting Magnet (SCM) in generating the precise magnetic field required to guide the electron beam for ECRH/ECCD in fusion reactors (from [7]).

The dimensions of the superconducting magnets in gyrotrons are comparable to the dimensions used in the pancake coil simulations presented in this thesis. This highlights the practical relevance of the simulated configurations for real-world devices.

1.2.2 Particle Accelerators

Superconducting magnets are also widely employed in particle accelerators to generate intense and precise magnetic fields required for beam steering and focusing. Notable examples include the Large Hadron Collider (LHC) at CERN and the European XFEL. These magnets must provide high field strength with extremely low losses, similar to the requirements in fusion devices. While the engineering context differs, the underlying superconducting technologies and challenges, such as current density limits and field quality, are closely related to the HTS coils studied in this thesis.

2 Numerical Modelling

Numerical modelling represents a powerful and indispensable tool for the simulation and analysis of High-Temperature Superconductor (HTS) behavior. This chapter provides a rigorous overview of the primary electromagnetic formulation employed for the analysis within this thesis: the $\mathbf{T} - \mathbf{A}$ formulation, which is implemented within the Finite Element Method (FEM) framework. The specific configuration and setup parameters adopted for this study, essential for modeling the nonlinear characteristics of HTS tape coils, are also detailed herein.

The formulation adopted in this study has been implemented using the commercial software *COMSOL Multiphysics®*.

2.1 The T-A Formulation

The T-A formulation is based on the idea of use the *current vector potential* $\vec{\mathbf{T}}$ and *magnetic vector potential* $\vec{\mathbf{A}}$ as state variables to solve the Maxwell equations (coupled with power law model), taking advantage of the high aspect ratio of the HTS tapes [13][1].

The peculiarity of this formulation is that the domain region is divided into two part and the solution comes from an iterative process that coupling them: in the superconductor region the state variable solved is T while, in all the domain region the state varible solved is A.

The definitions of the *current vector potential* $\vec{\mathbf{T}}$ and *magnetic vector potential* $\vec{\mathbf{A}}$ are the following:

$$\vec{J} = \nabla \times \vec{\mathbf{T}} \qquad \vec{B} = \nabla \times \vec{\mathbf{A}} \tag{2.1}$$

The superconductor is modelled as an infinitely thin layer: the current is constrained to flow within the sheet and the current vector potential T is always perpendicular to the superconductor.

The governing equation in the superconductor region (*T-Formulation*) is:

$$\nabla \times (\rho \nabla \times \vec{\mathbf{T}}) = -\frac{\partial \vec{B}}{\partial t} \tag{2.2}$$

Where the resistivity ρ is modelled with the *power law model* as in (1.1) and the magnetic field intensity $\vec{B}$ is obtained from the *A-Formulation* (applied in all the domain) through the following equation:

$$\nabla \times \vec{B} = \mu \vec{J} \tag{2.3}$$

with the boundary condition to impose the current:

$$I = \iint_S \vec{J} dS = \iint_S (\nabla \times \vec{\mathbf{T}}) dS = \oint_{\partial S} \vec{\mathbf{T}} dr \tag{2.4}$$

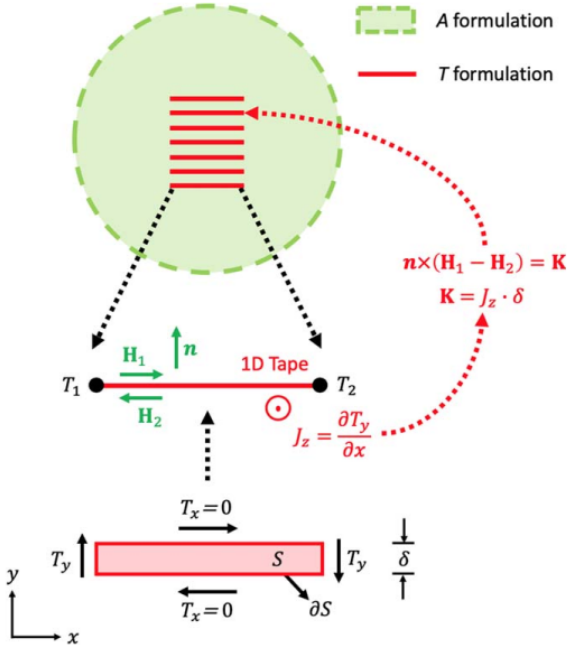

Figure 2.1: Schematic representation of the **T** − **A** Formulation, showing the current vector potential (**T**) applied in the superconducting domain and the magnetic vector potential (**A**) applied across the entire domain, coupled by boundary conditions on the magnetic field (**H**) and the surface current density (**K**). (from [1]).

In this thesis, only the 2D case (axisymmetric) is considered, for this reason the equation can be simplified as follow (refer to figure 2.1). Eq (2.2) and eq (2.3) become:

$$\frac{\partial}{\partial x}\left(\rho\frac{\partial T_y}{\partial x}\right) = \frac{\partial B_y}{\partial t} \tag{2.5}$$

$$\nabla^2\mathbf{A} = \mu J_z \tag{2.6}$$

and the B.C, is:

$$I = (T_2 - T_1)\delta \tag{2.7}$$

where δ is the thickness of the HTS tape. A *Surface current density* $\vec{K} = \vec{J_z} \cdot \delta$ [A/m] is introduced to be inserted in the A formulation by the boundary condition:

$$\hat{n} \times (\vec{H_1} - \vec{H_2}) = \vec{K} \tag{2.8}$$

where:

- $\vec{n}$ is the normal unit vector respect to the tape surface;
- $\vec{H_1} - \vec{H_2}$ is the difference between the magnetic field strength vector parallel to the tape.

T-A Homogeneous approach

The *T-A Homogeneous approach* consist in considering the stack of HTS as an homogeneous bulk increasing the simplicity of the geometry and reducing the computational effort and consequentially time.

As in the full model, the magnetic field B parallel to the tape has no influence inside the superconductor and T has only one component. The boundary condition 4.12 is now applied to the edge (with normal vector $\vec{n}$) and a new Neumann B.C. is required:

$$\frac{\partial T_y}{\partial \vec{n}} = 0 \tag{2.9}$$

In order to model properly the input current inside the SC domain, the current density needs to be reduced by the so called *homogenization factor* h_f:

$$h_f = \frac{\delta}{\Lambda} \rightarrow J_h = h_f J_z \tag{2.10}$$

where δ is the thickness of the tape, Λ is the thickness of the unit (the total width of the coil divided by the number of turns).

In the mathematical formulation, the T-A homogeneous model is the same of the full model.

2.2 Simulation Setup

In this section, there will be a resume of the general parameters set in the COMSOL platform to carry out the simulations.

2.2.1 High Temperature Superconductor tape specifics

The table 2.1 shows the geometric parameter refered to the modelled HTS tape. These parameters correspond to typical 2G-HTS (second generation HTS).

Parameter	Value	Unit
Tape width	0.004	m
Tape hight	5.7143×10^{-5}	m
HTS layer hight	10^{-6}	m
$I_{c0}(20K)$	2196	A
Power Law Index (n)	25	1

Table 2.1: Geometric and electrical parameters for the simulated 2G-HTS (REBCO) tape, including layer thickness, tape width, and self-field critical current (I_{c0} at 20 K)14.

2.2.2 Critical Current density model

To model the influence of magnetic field on the critical current density $J_c(\vec{B})$, the extended Kim model is used [14].

The relation between magnetic field and critical current density is:

$$J_c(B,\theta) = J_{c0}\left(1+\epsilon_\theta\left(\frac{B}{B_0}\right)^{\alpha}\right)^{-\beta} \tag{2.11}$$

with the Blatter's angular anisotropy factor expressed by:

$$\epsilon_\theta = \sqrt{\gamma^{-1}cos^2(\theta) - sin^2(\theta)} \tag{2.12}$$

The parameters β and B_0 are related to the thermally activated flux-creep processes and I_{c0} is the self-field critical current density.

The angle θ is the angle between the flat surface of the HTS and the magnetic field direction (see fig 2.2a).

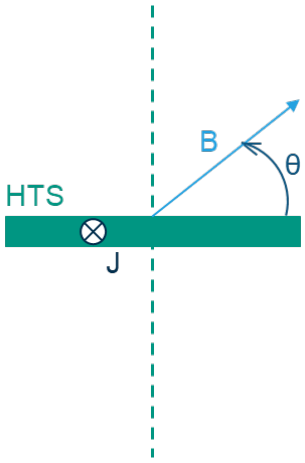

(a) Orientation of the field angle and the direction of the transport current.

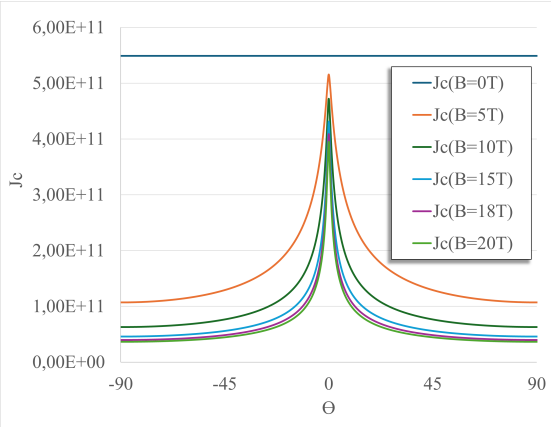

(b) Plot of J_{c0} and $J_c(B,\theta)$.

Figure 2.2: The magneto-angular dependence of the critical current density, $J_c(\mathbf{B},\theta)$, as modeled by the Extended Kim Model (using parameters from Table 2.2). (a) Orientation of the magnetic field vector ($\mathbf{B}$) relative to the flat surface of the HTS tape (angle θ). (b) Resulting J_c profile showing sensitivity to the field angle.

In the following analysis the parameters used to model the critical current density are expressed in table 2.2.

2.2.3 Pancake Coils Parameters

The case study is based on a 2D axisymmetric formulation. To reduce computational cost, an additional symmetry axis is introduced in the radial direction. Consequently,

Parameter	Value	Unit
J_{c0}	5.49×10^{-11}	A/m^2
B_0	0.6736	T
γ	18490	1
α	1.368	1
β	0.5829	1

Table 2.2: Parameters used in the Extended Kim Model to define the magneto-angular dependence of the critical current density $J_c(\mathbf{B}, \theta)$[14].

simulations involving multiple pancakes must be mirrored and revolved to reconstruct the full coil geometry (see Figure 2.3). From an electrical standpoint, all coils are considered perfectly insulated, and all pancakes are connected in series, with each turn and each pancake carrying the same transport current.

The pancakes coil parameter are listed in the table 2.3 .

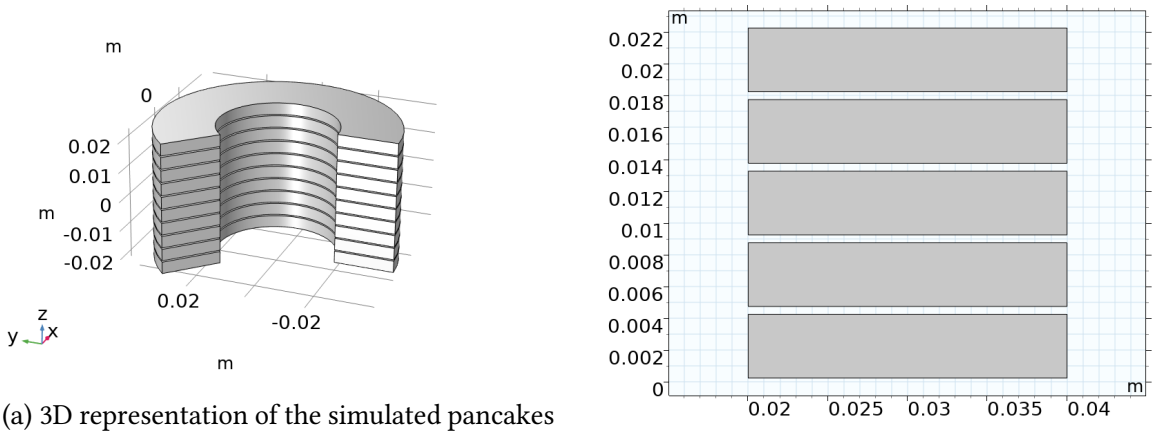

(a) 3D representation of the simulated pancakes coil.

(b) Simulated HTS domain.

Figure 2.3: Transition from the full 3D geometry (a) to the computationally efficient 2D axisymmetric domain (R-Z plane) (b). The simulated 90° quadrant (R-Z plane) is revolved and mirrored to represent the full coil geometry.

Parameter	Value	Unit
Number of pancakes	1 to 10	1
Turns/Pancake	350	1
Gap between pancakes	0.0005	m
Inner radius	0.02	m
Outer radius	0.04	m

Table 2.3: Key geometric and electrical parameters for the tested HTS pancake coil configurations (1 to 10 Pancakes)

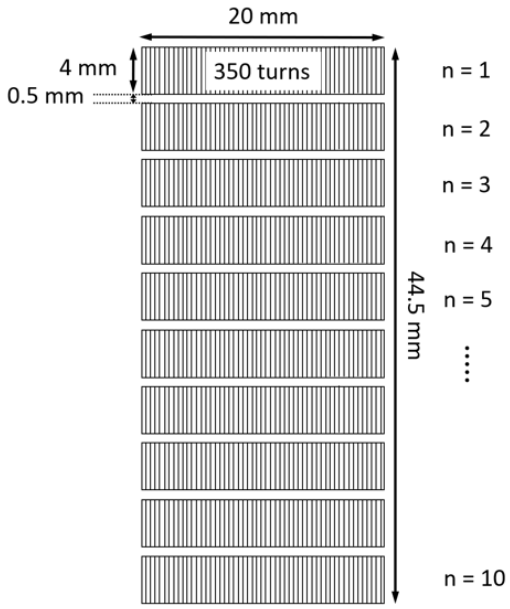

Figure 2.4: Detailed geometry of the simulated **10**-pancake stack in the 2D domain, illustrating the inner radius (20 mm), outer radius (40 mm), tape width (4 mm), and the inter-pancake gap (0.5 mm).

2.2.4 Mesh building

After different tests, a good compromise between computational time and accuracy of the results is obtained with the following mesh refinement at the boundary of the pancakes:

- 30 elements for each pancake in the z-direction with linear symmetric growth rate.
- 20 elements for each pancake in the r-direction with linear symmetric growth rate.

The resulting mesh in the pancake region is made up of 600 rectangular elements; the linear growth rate distribution is chosen to improve the refinement close to the boundary.

In the air domain region, a free triangular mesh is chosen.

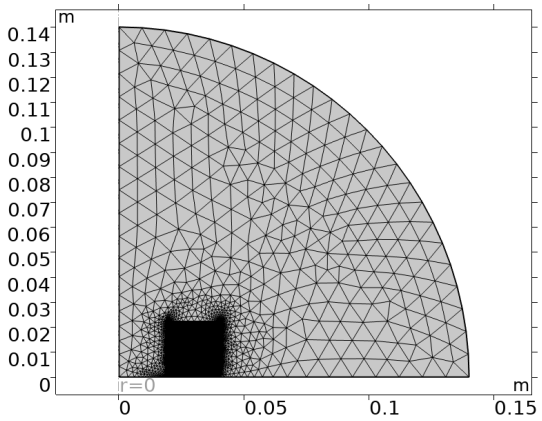

Figure 2.5: Overview of the Finite Element Method (FEM) mesh across the entire simulation domain, including the air domain and the superconducting region.

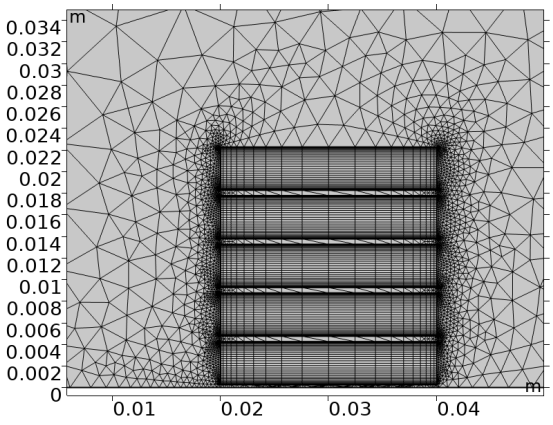

Figure 2.6: Detailed view of the structured mesh refinement applied specifically within the active HTS regions, utilizing more refined rectangular elements to enhance accuracy near the boundaries where field and current gradients are highest.

3 Simulations Results

3.1 Electromagnetic Analysis of a single pancake coil

The first set of simulations focuses on the analysis of a single pancake coil, with geometric and electrical parameters reported in chapter 2 section 2.2. The study initially investigates the current distribution within the pancake cross-section and the reduction of the critical current caused by the self-induced magnetic field.

Subsequently, methods for determining the maximum allowable input current are presented. Once this value is established, the analysis proceeds to examine the time evolution of the current distribution and to evaluate the quality of the resulting magnetic field.

3.1.1 Current Density Distribution in one pancake coil

The first analysis is conducted by applying a current ramp from 0 to 1000 A with a ramp rate of 1 A/s (fig. 3.11), significantly below the theoretical maximum critical current of the superconductor, which is approximately 2196 A. This approach allows the observation of the current behavior within the pancake coil cross section.

The resulting plots 3.2 show the azimuthal current density (J_ϕ) normalized on the value of the local critical current density across the pancake cross-section at different values of the input current peak, providing insight into how the current distributes itself.

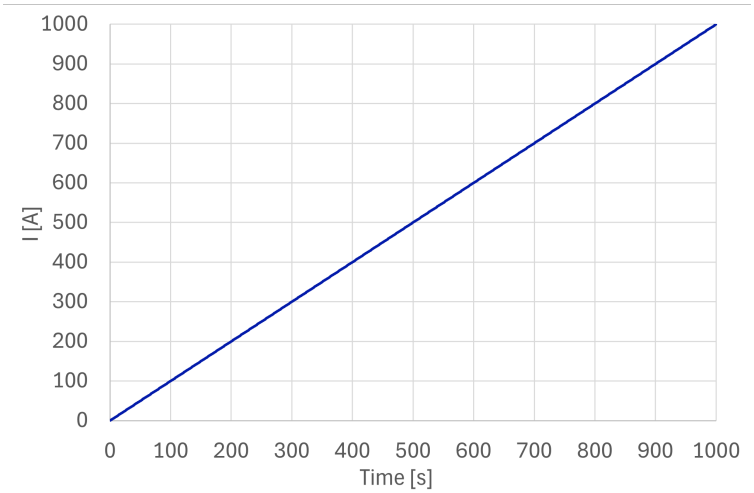

Figure 3.1: Input current profile used for the electromagnetic analysis of the single-pancake coil, showing the linear ramp-up phase (Ramping rate: 1 A/s).

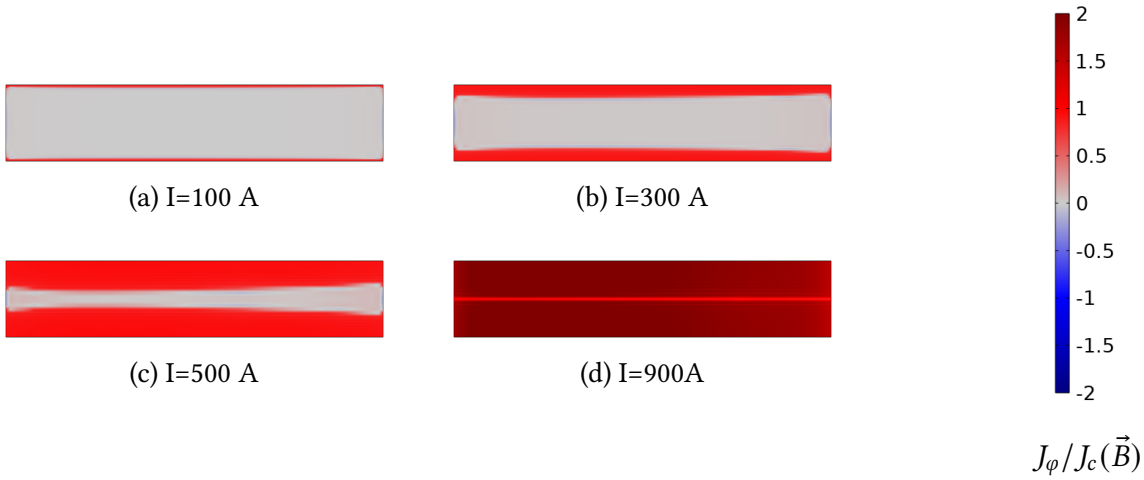

(a) I=100 A (b) I=300 A

(c) I=500 A (d) I=900A

Figure 3.2: Distribution of normalized azimuthal current density ($J_\varphi / J_c(\mathbf{B})$) across the single-pancake cross-section at increasing input current levels, illustrating the penetration of the magnetic flux.

The following plots (Figure 3.3) illustrate the reduction of the critical current density caused by the self-induced magnetic field in the superconductor at different time instants. These results provide a clearer understanding of the resulting current distribution, highlighting how the upper and lower regions of the pancake coil experience a decrease in critical current density due to the presence of a magnetic field component perpendicular to the tape surface, as also evidenced by the radial magnetic field distribution shown in Figure 3.4.

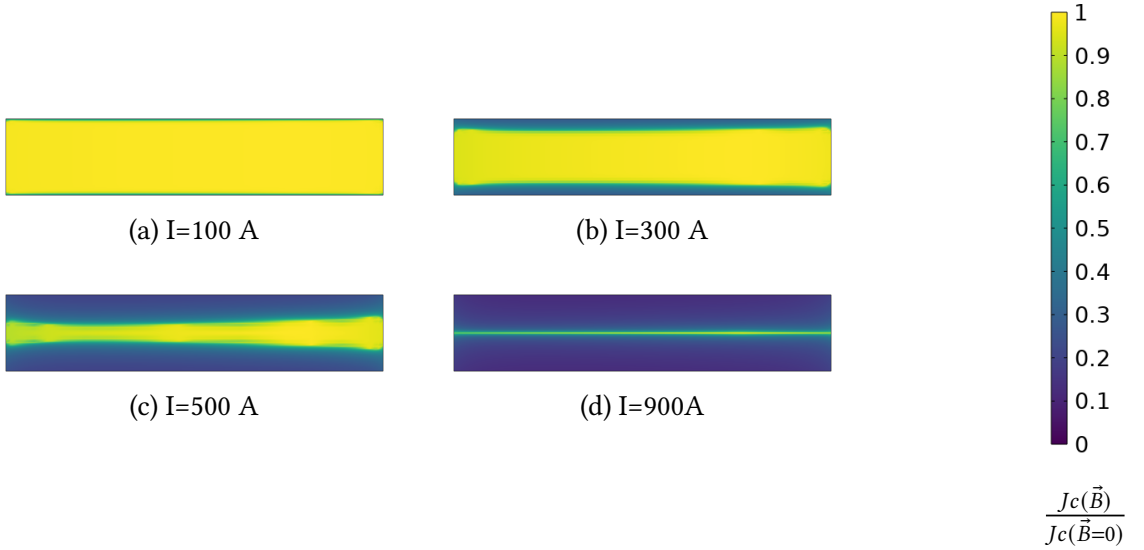

(a) I=100 A (b) I=300 A

(c) I=500 A (d) I=900A

Figure 3.3: Reduction factor of the critical current density ($J_c(\mathbf{B})/J_{c0}$) in the single-pancake cross-section, showing the local degradation of superconducting capacity induced by the self-field ($\mathbf{B}$) as the transport current increases.

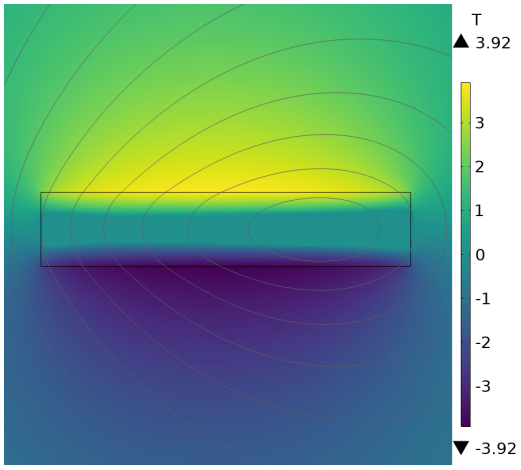

Figure 3.4: 2D plot of the radial magnetic field component (B_r) generated by the single-pancake coil at $I = 500$ A. The presence of B_r perpendicular to the tape surface is the primary cause of J_c degradation near the tape edges.

Determination of the Maximum Input Current

The influence of magnetic field on the critical current density reduce the maximum input current. It is necessary to establish a method for determining the maximum input current in the pancake coil configuration.

Due to the simplicity of the single-pancake configuration, it is possible to simulate each discrete turn of the coil. A convenient method to determine the maximum allowable input current is the *load line method*.

For the single-pancake case, the relatively low computational cost makes it feasible to compute the integral of the critical current density for each turn at different input current values.

Figure 3.5 shows the resulting load lines, where the line with the minimum intersection represents the critical turn and defines the maximum operating current of the coil.

The resulting maximum input current obtained from the load line method is approximately 589 A. To verify the validity of this approach, the classical experimental procedure (described in [9]) was reproduced within the simulation to determine the critical current. As shown in Figure 3.7, according to the electric field criterion, the current value at which the electric field reaches 10^{-4} V/m is approximately 580 A, in agreement with the value obtained from the load line method.

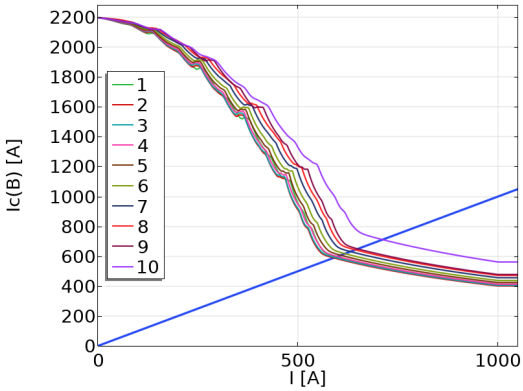

(a) Load line Method one-pancake, ten turns Ic plotted.

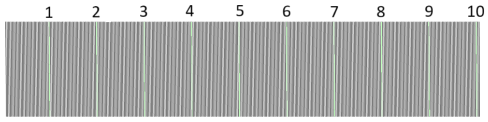

(b) In green the ten turns taking in account.

Figure 3.5: Load Line Method for the single-pancake coil: (a) Intersection of the current demand line and the critical current curves ($I_c(\mathbf{B})$) for selected turns, defining the Maximum Operating Current ($I_{\max}$). (b) Schematic showing the 10 representative turns used for the discrete analysis.

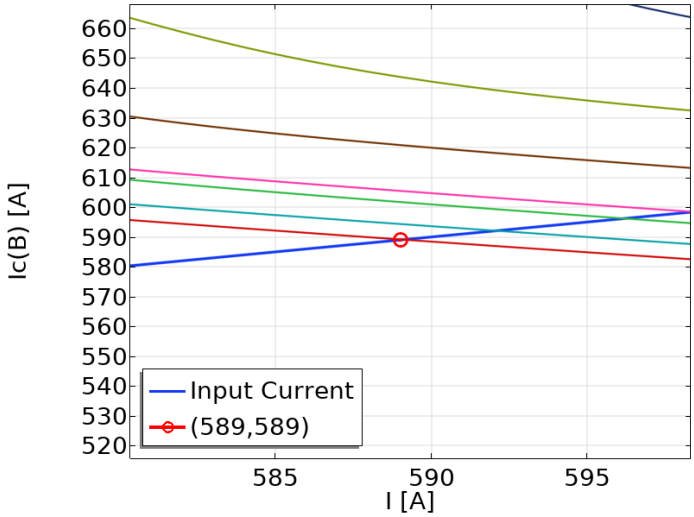

Figure 3.6: Zoomed view of the Load Line intersection, confirming the precise determination of the Maximum Operating Current ($I_{\max}$) where the most critical turn transitions out of the superconducting state.

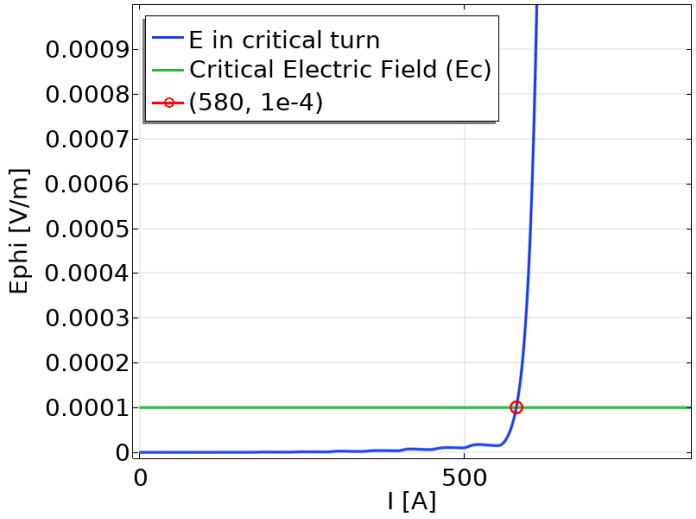

Figure 3.7: Simulated electric field (E_φ) vs. transport current (I) curve for the critical turn, verifying the Maximum Operating Current ($I_{\max}$) using the standard E-field criterion ($E_c = 10^{-4}$ V/m).

3.1.2 Magnetic Field Quality in one pancake coil

The analysis proceeds by considering approximately 70% of the maximum input current determined from the load line method. The input current is defined as a linear ramp starting from $t = 0$ s, increasing at a rate of 1 A/s until reaching a value of 415 A (Fig. 3.8). The simulation is subsequently continued for a total duration equal to three times the ramp period, in order to allow for current relaxation and stabilization of the electromagnetic field distribution.

To investigate the magnetic field quality, the simulated case is compared with another simulation in which a uniform current distribution is imposed throughout the pancake cross section, while keeping all geometric parameters unchanged. From both a qualitative assessment (Fig. 3.9) and a quantitative investigation (Fig. 3.10), it can be observed that, in the case of a single pancake, the magnetic field generated by the insulated HTS coil is almost identical to that produced by a pancake with a uniform current distribution.

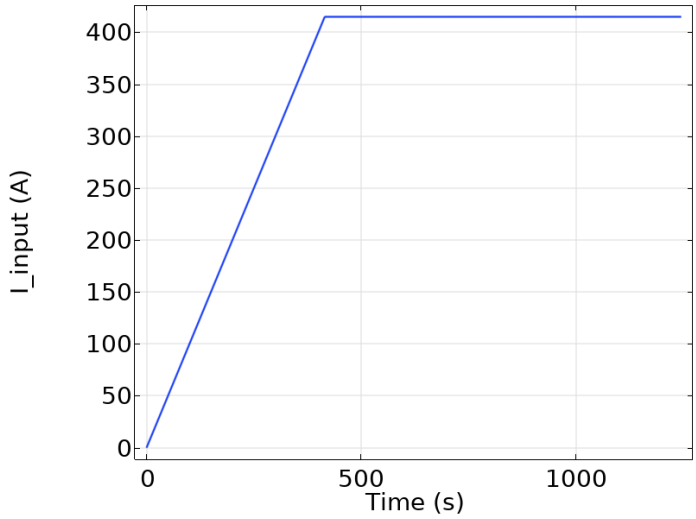

Figure 3.8: Input current profile used for the Field Quality evaluation in the single-pancake coil, set to 70% of I_{max} (415 A), followed by a prolonged steady-state period to observe current relaxation.

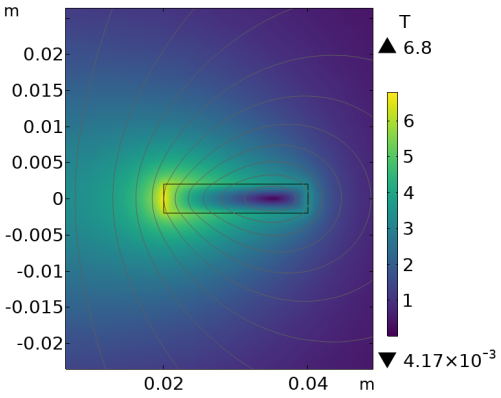

(a) Magnetic Field norm with T-A formulation

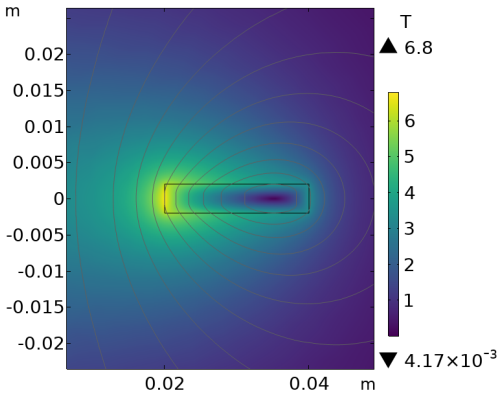

(b) Magnetic Field norm with uniform current distribution

Figure 3.9: Comparison of the magnetic field magnitude ($|\mathbf{B}|$) distribution between (a) the HTS simulation (T-A formulation) and (b) the ideal uniform current distribution, showing minimal deviation for the single-pancake case.

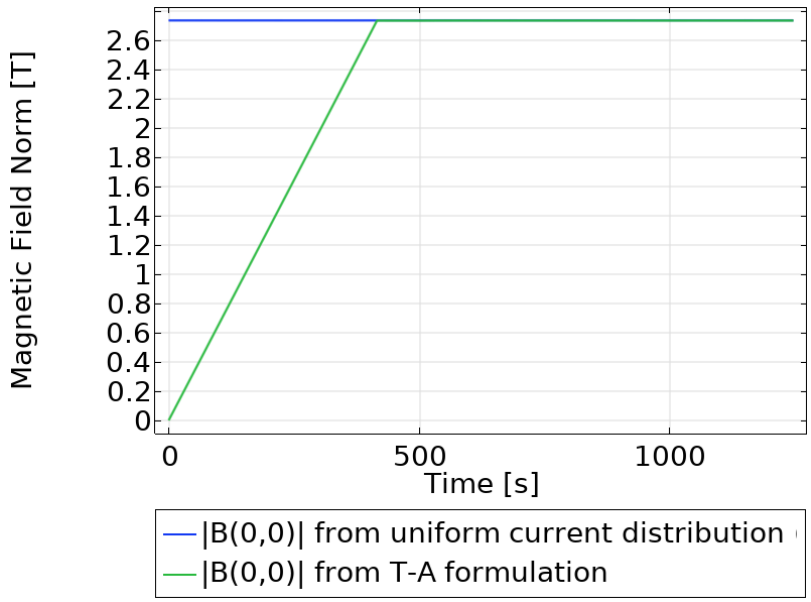

Figure 3.10: Time evolution of the magnetic field norm at the coil center ($|\mathbf{B}(0,0)|$), comparing the HTS simulation (T-A) against the ideal uniform model, confirming high fidelity in the single-pancake case.

3.2 Electromagnetic Analysis of Multiple Pancake Coils

In this investigation, the number of pancakes is increased in order to study how this affects the electromagnetic behavior. Compared to the previous analysis (Section 3.1), the homogeneous model is adopted to reduce the computational effort (a further validation of this model for the present setup is reported in Appendix **??**). Moreover, an additional symmetry axis is introduced at $r = 0$.

3.2.1 Current Density Distribution in four pancakes coils

Using a current ramp of 1 A/s with the same maximum current value as in the single-pancake case, the stronger self-generated magnetic field and the greater influence of the radial field component on the outer pancakes lead to a faster saturation of the current distribution in those regions, due to a more pronounced reduction of the critical current (see fig. 3.13). From Figure 3.12, it can be observed that the local current density exceeds the critical current density even before the end of the ramp.

By increasing the number of pancakes, the screening current phenomenon becomes more pronounced (highlighted in blue in the figure 3.12). These magnetization currents, induced within the superconducting layer with opposite polarity to the transport current, act to shield the internal magnetic field, leading to a partial reduction of the effective field in the coil bore.

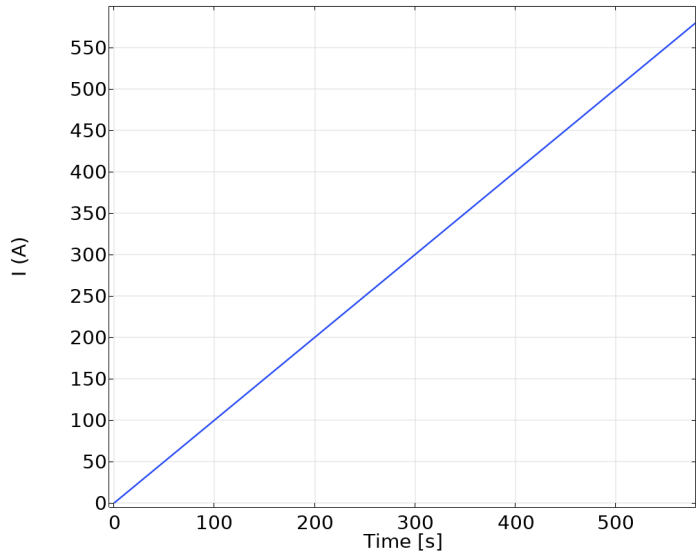

Figure 3.11: Input current profile used for the electromagnetic analysis of the four-pancake stack.

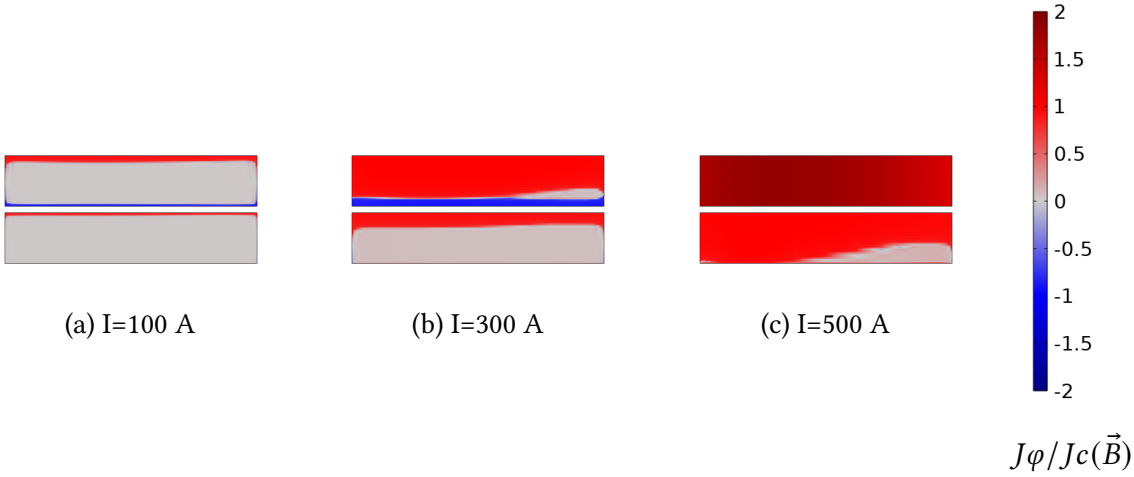

(a) I=100 A (b) I=300 A (c) I=500 A

Figure 3.12: Distribution of normalized current density ($J_\varphi/J_c(\mathbf{B})$) in the four-pancake stack at increasing input currents, highlighting the more pronounced SCIF and non-uniform current penetration compared to the single-pancake case.

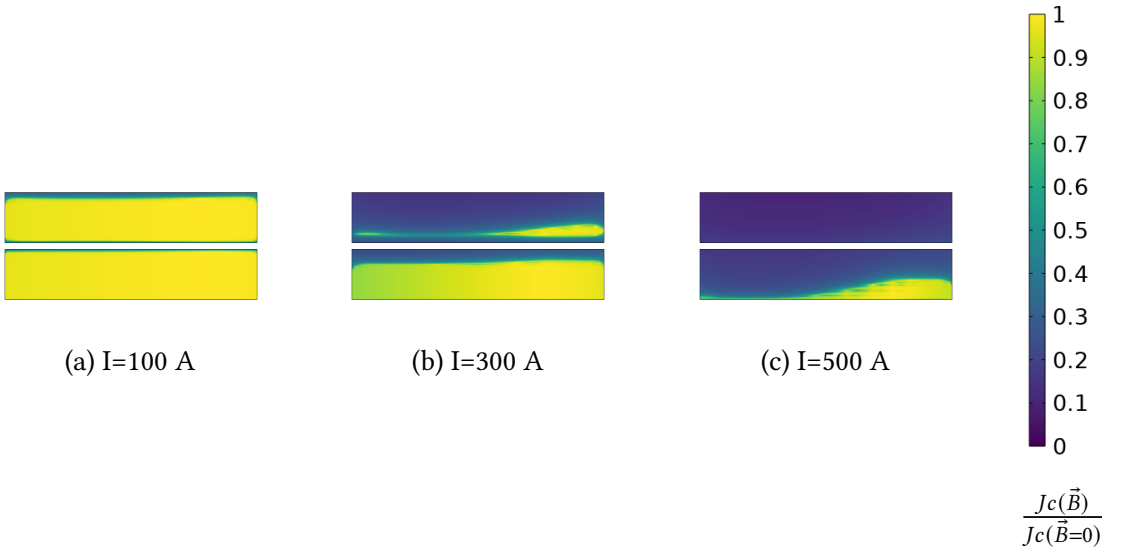

(a) I=100 A (b) I=300 A (c) I=500 A

Figure 3.13: Reduction factor of the critical current density ($J_c(\mathbf{B})/J_{c0}$) in the four-pancake stack, showing greater local degradation due to increased self-field interaction between the pancakes.

Determination of the Maximum Input Current

In this case, the method adopted to determine the maximum allowable input current for the pancake coil system is the load line method, taking into account the integral of the current density over the cross-section of each pancake. This procedure yields an average critical current for each pancake at every input current value between 1 and 600 A. As expected, the minimum intersection point with the current ramp corresponds to the curve representing the outermost pancake, which occurs at approximately 378 A (see fig. 3.14). The following analysis will be performed taking into account 70% of this value.

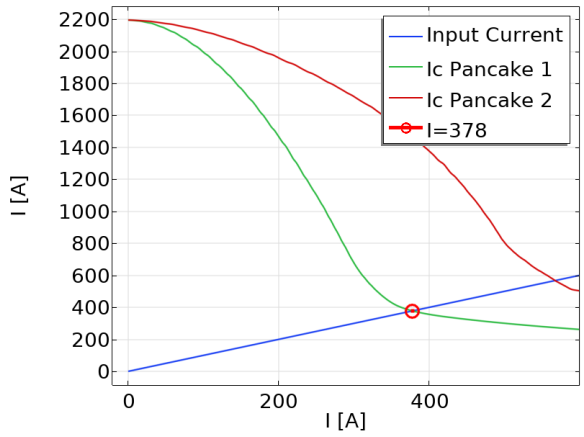

Figure 3.14: Load Line Method for the four-pancake stack. The intersection point defines $I_{\max} \approx 378$ A, which is significantly lower than the single-pancake case due to stronger mutual inductance effects.

3.2.2 Electromagnetic Behavior of a Four-Pancake Coil

The analysis on the 4-pancake configuration will be carried out by applying a current ramp of 1 A/s, which will stop at 264 A (70% of the maximum input current), in order to evaluate the characteristics of the resulting current distribution.

After reaching the maximum current, the simulation is extended up to t =1000s in order to capture the relaxation phenomena and the subsequent redistribution of the current within the pancake (fig. 3.15).

The relaxation process leads to a progressive increase in current penetration within the superconductor. This effect has a beneficial impact on the operating margin with respect to the critical current density, as the broader spatial distribution of current results in a reduction of the local current density, thereby increasing the distance from the critical threshold (figures 3.16a and 3.16a). Figures 3.16b and 3.17b qualitatively assess the influence of the current distribution on the spatial profile of the magnetic field magnitude.

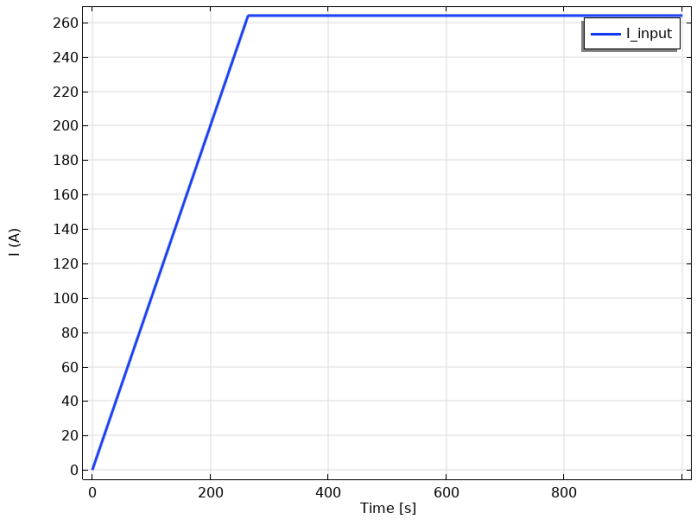

Figure 3.15: Input current profile used for the Field Quality evaluation in the four-pancake stack, set to 70% of I_{max} (264 A), followed by a steady-state period to analyze relaxation.

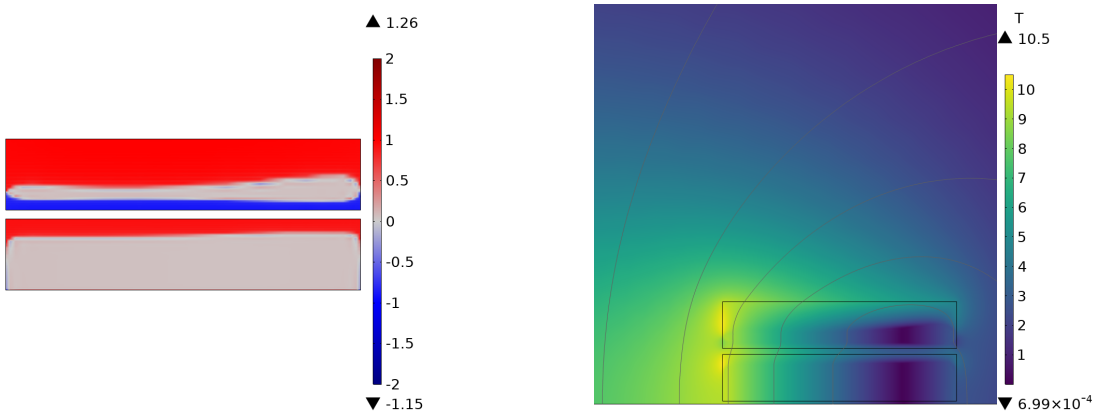

(a) (b)

Figure 3.16: (a) Normalized current density distribution at the peak current ($t = 264$ s) showing pronounced SCIF effects (blue regions). (b) Corresponding magnetic field norm distribution ($|\mathbf{B}|$[T]).

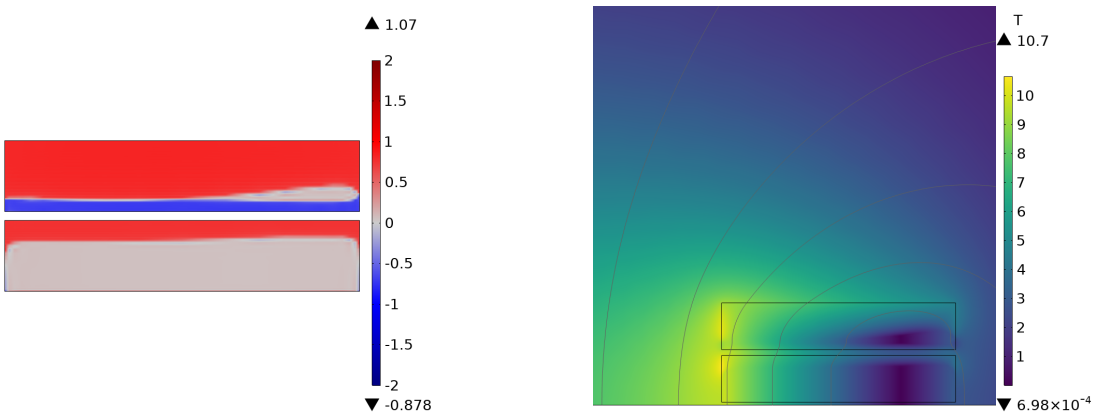

(a) (b)

Figure 3.17: (a) Current density distribution during the steady-state phase ($t = 1000$ s), showing current relaxation and further penetration which reduces local current density and field non-uniformity. (b) Corresponding magnetic field norm distribution.

3.2.3 Quality Field Evaluation

A simulation with an ideal uniform current distribution is used as a reference to evaluate the magnetic field quality generated by the four-pancake HTS model. The figures (3.18a) show a qualitative difference between the ideal model and the HTS one. Subsequently, a more quantitative analysis is performed, focusing on the differences observed at the center point (fig. 3.19). In this case, a deviation arises compared to the single-pancake case, mainly due to the more complex current distribution and the effect of the screening currents, that can be quantifies as:

$$\begin{aligned} B_{\mathrm{SC}}(0,0) &= B_{\mathrm{HTS}}(0,0) - B_{\mathrm{id}}(0,0) \\ B_{\mathrm{SC}} &= 7.20 - 7.28 = -0.08\ \mathrm{T} \quad \text{when } t = 264\ \mathrm{s} \\ B_{\mathrm{SC}} &= 7.25 - 7.28 = -0.03\ \mathrm{T} \quad \text{when } t = 1000\ \mathrm{s} \end{aligned} \tag{3.1}$$

For this reason, additional analyses along the mid-plane (fig. 3.21) and center line (fig. 3.20) are presented to gain a deeper understanding of the spatial variations in the magnetic field magnitude. The mid-plane line is defined as 80% of the inner radius and the center line is 150% the half height of the stack.

From figure 3.21 the effects of *field drift* can be appreciated. Figure 3.31 illustrates the effect of field drift on the magnetic field quality. In particular, the field drift results in a magnetic field magnitude that more closely resembles the ideal field produced by a uniform current distribution.

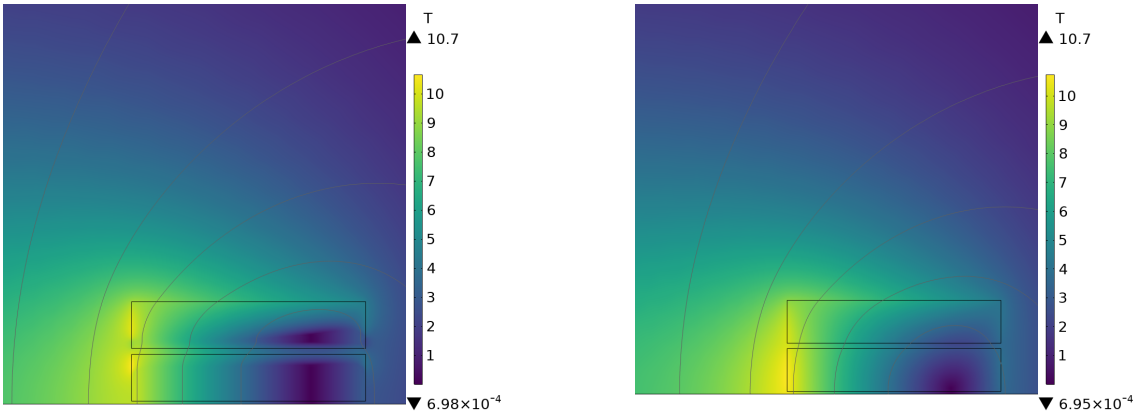

(a) |B(r,z)| HTS

(b) |B(r,z)| Ideal

Figure 3.18: Comparison of the magnetic field magnitude ($|\mathbf{B}(r,z)|$) distribution between (a) the HTS simulation and (b) the ideal uniform current distribution, clearly showing initial SCIF distortion in the HTS field profile.

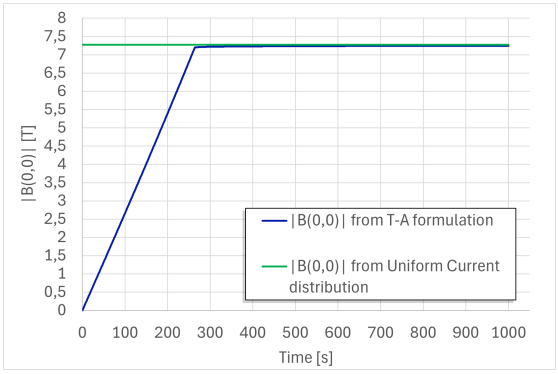

(a) Comparison of magnetic field norm in the center point.

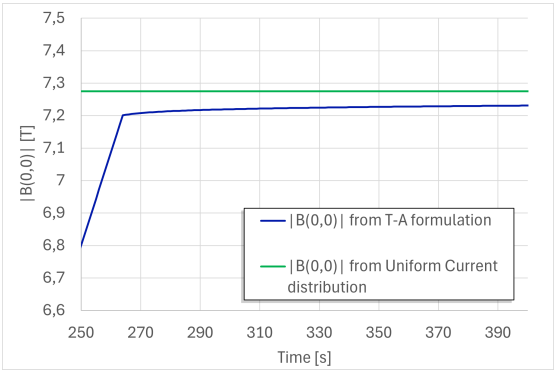

(b) Zoomed view of the magnetic field norm in the center point.

Figure 3.19: (a) Time evolution of the magnetic field norm at the center point ($|\mathbf{B}(0,0)|$) comparing HTS and ideal models. (b) Zoomed view, quantifying the SCIF-induced magnetic field deficit and subsequent relaxation (field drift).

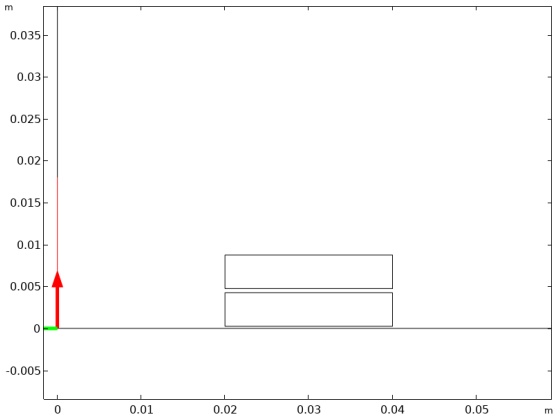

(a) The red line represent the arc length for this quality field evaluation.

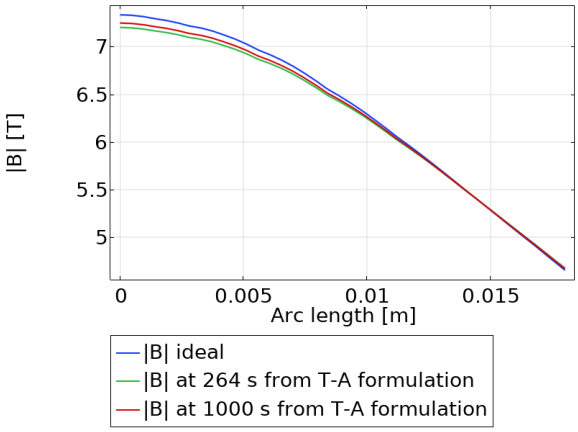

(b) Magnetic field norm in ideal case, HTS simulation at the peak and HTS simulation at the end.

Figure 3.20: Magnetic field norm profile along the center line of the 4-pancake coil, comparing the ideal case ($|\mathbf{B}|$ ideal) against the HTS simulation at ramp peak ($t = 264$ s) and during relaxation ($t = 1000$ s).

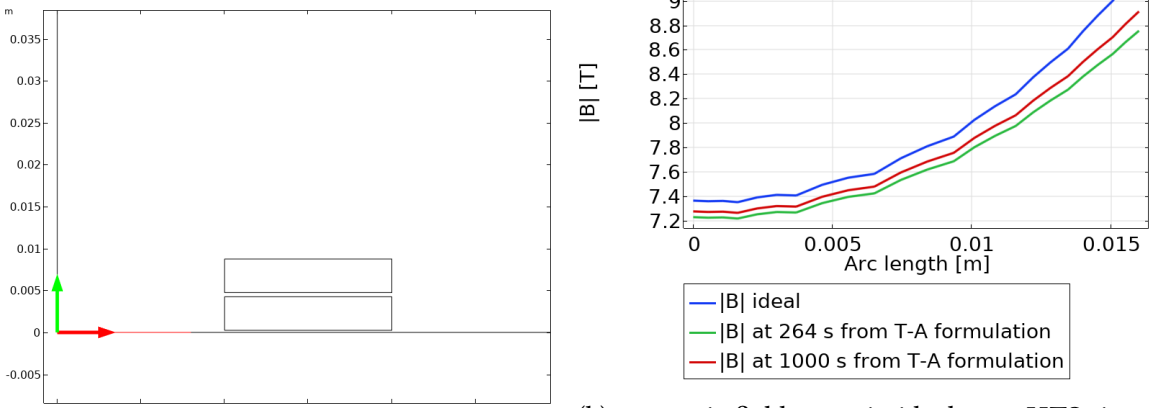

(a) The red line represent the arc length for this quality field evaluation.

(b) magnetic field norm in ideal case, HTS simulation at the peak and HTS simulation at the end.

Figure 3.21: Magnetic field norm profile along the middle-plane of the 4-pancake coil, illustrating the effect of current relaxation on improving field quality over time.

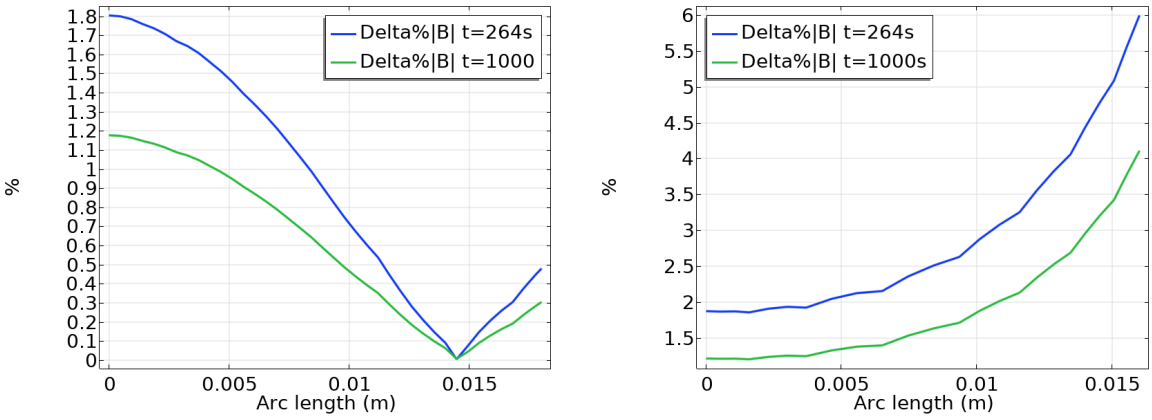

(a) (b)

Figure 3.22: Relative percent difference (ϵ) in magnetic field norm ($|\mathbf{B}|$) between the HTS simulation and the ideal model ($\epsilon = \frac{|B_{\text{HTS}} - B_{\text{id}}|}{B_{\text{id}}} \times 100$) along the center line (a) and the middle-plane (b), quantifying the spatial extent of the SCIF degradation.

3.3 Ten Pancake Coils simulation

In this section a configuration of 10-pancake coils is analyzed. Also in this case, the simmetric axis cut the stack of pancake in an half resulting in five pancake cross sections images. As was done before, the analysis starts with some consideration about the determination of the maximum input current: First of all a current ramp from 0 A to 377 A (the value of the critical current for four-pancake configuration) will be set in order to conclude that adding pancakes results in a lower maximum input current. Then, when the value of the current peak will be find, a series of simulation will be carried out to make some consideration about the current density distribution and the field quality.

3.3.1 Maximum input current in 10 Pancake coils

Starting with an input current ramp from 0 A to 377 A (fig. 3.23) can be seen how the distribution of current lead to a non superconducting zone (with $J_\varphi / J_c > 1.2$). To determine the maximum input current the load line method in this case represent the plot of the average critical current in each pancakes. The minimum intersection regard the top (bottom) pancake (fig. 3.25) which intersects the load line at the value of 308 A .

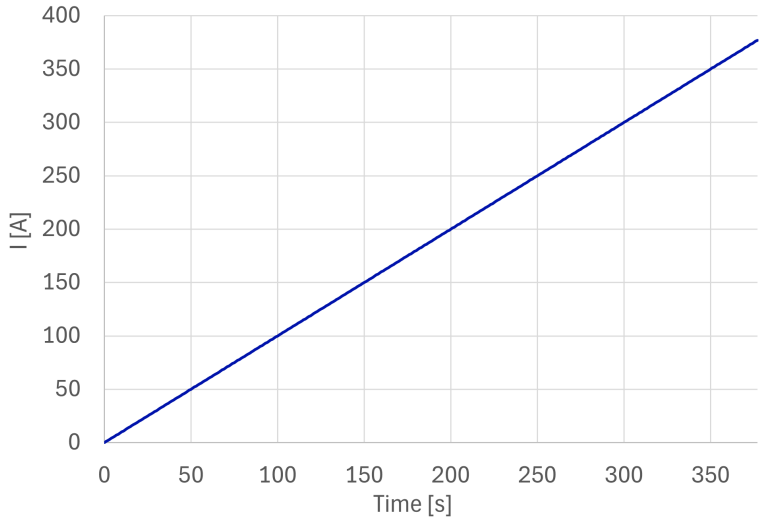

Figure 3.23: Input current profile used to determine the Maximum Operating Current ($I_{\max}$) for the 10-pancake stack via the Load Line Method.

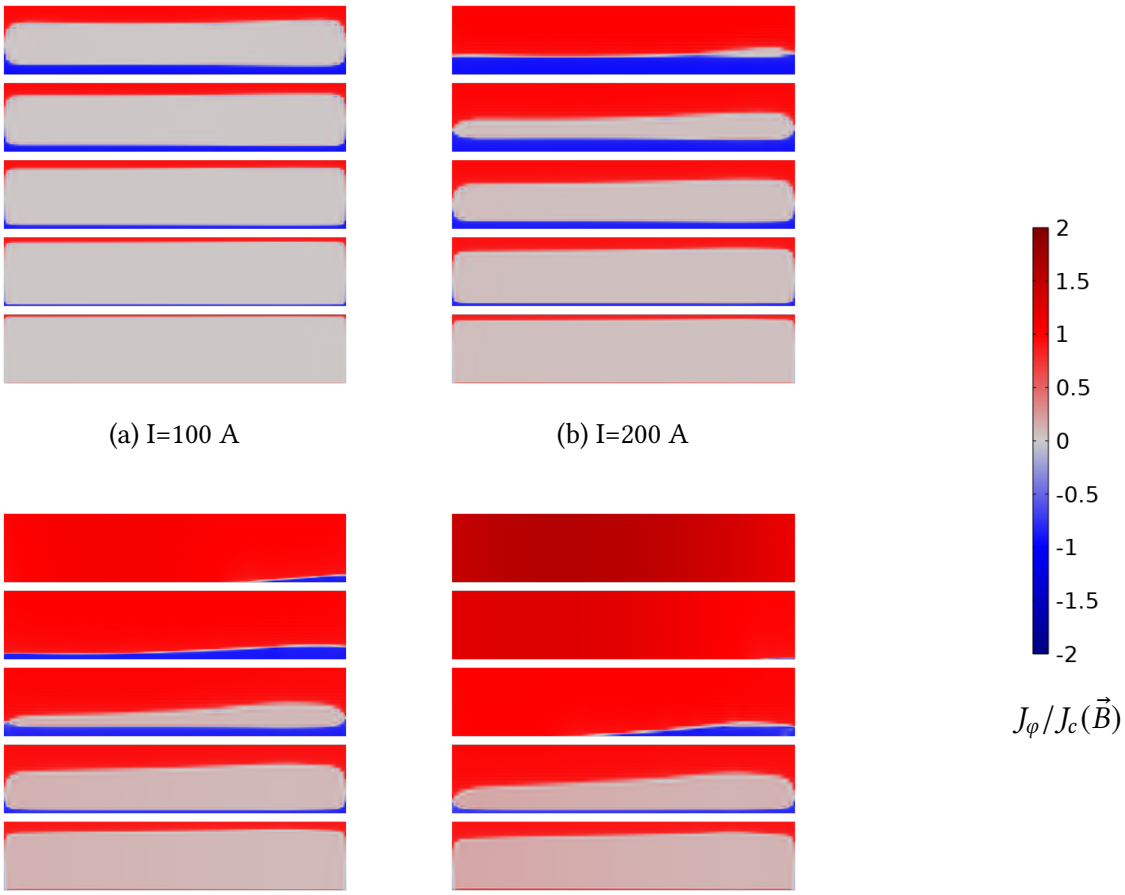

(a) I=100 A

(b) I=200 A

(c) I=300 A

(d) I=377A

Figure 3.24: Distribution of normalized current density ($J_\varphi/J_c(\mathbf{B})$) in the 10-pancake stack at high input currents, clearly showing the failure mode where J_φ/J_c exceeds 1.

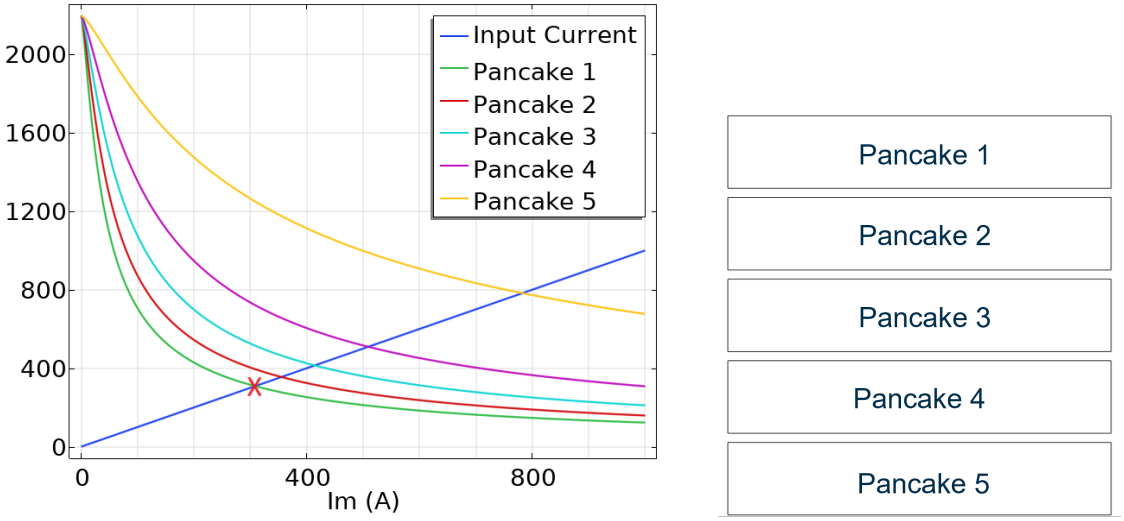

(a) (b)

Figure 3.25: Load Line Method for the 10-pancake stack. (a) Critical current curves for each pancake (labeled 1-5, with symmetry assumed) and the intersection point determining $I_{\max} \approx 308$ A. (b) Schematic labeling of the five pancakes used in the axisymmetric simulation.

3.3.2 Screening currents and Quality field evaluation

Taking into account the 70% of the maximum input current found previously, the analysis goes on. The new current peak now is $0.7 \cdot 308 = 216$ A. The value of 216 A is reached at the time 216 s as shown in 3.26.

The two most relevant time instants in the simulation are identified as follows:

- **t = 216 s**: this corresponds to the end of the current ramp, when the input current reaches its peak value. It represents the most critical phase of the simulation, as the current has not yet relaxed and local losses of superconductivity may occur (see fig. 3.27).
- **t = 650 s**: at this time (approximately three times the ramp duration), the system reaches a steady-state configuration, representative of the normal operating condition of the magnet(see fig. 3.28).

The evaluation of the Screening Current Induced Field (B_{SC}) in the center point can be extracted from 3.29 and qunatified as follow:

$$\begin{aligned} B_{SC}(0,0) &= B_{HTS}(0,0) - B_{id}(0,0) \\ B_{SC} &= 12.08 - 12.65 = -0.57 \text{ T} \quad \text{when } t = 216 \text{ s} \\ B_{SC} &= 12.20 - 12.65 = -0.45 \text{ T} \quad \text{when } t = 650 \text{ s} \end{aligned} \tag{3.2}$$

. The magnitude of the magnetic field induced by the screening currents becomes more pronounced in the 10-pancake coil configuration compared to the 4-pancake case. As

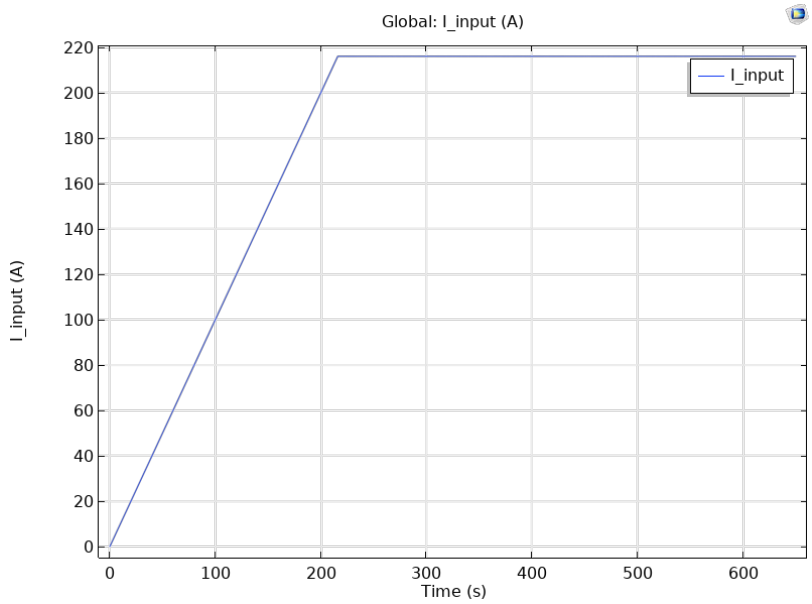

Figure 3.26: Input current profile used for the Field Quality evaluation in the 10-pancake stack, set to 70% of I_{max} (216 A), followed by a steady-state period.

shown in Figure 3.28a, the screening currents (highlighted in blue) play a significantly more prominent role in this configuration. From the comparative analysis of the single-pancake, 4-pancake, and 10-pancake coils, a clear trend can be observed: as the number of pancakes increases, the intensity of the screening currents rises, leading to a progressive degradation of the magnetic field quality due to the stronger Screening Current Induced Field (SCIF).

The same conclusion can be seen by watching on the relative error of the magnetic field of the HTS to respect the ideal magnetic field in the middle plane line and center line from the figures 3.31a and 3.21a.

To get more information about the magnetic field distribution, the figures 3.30 offer a prospective on the behavior of the magnetic field along the middle plane line and center line.

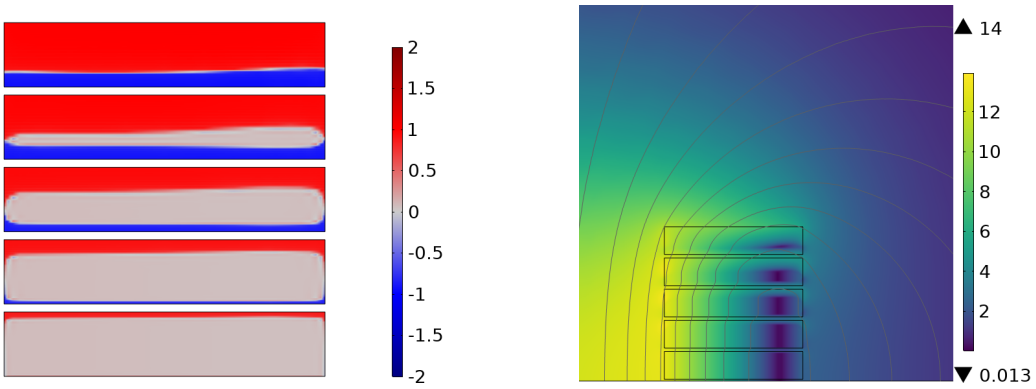

(a) (b)

Figure 3.27: (a) Normalized current density distribution at the peak current (t = 216 s), showing the extensive penetration of the current front and the large SCIF regions. (b) Corresponding magnetic field norm distribution (|**B**|[T]).

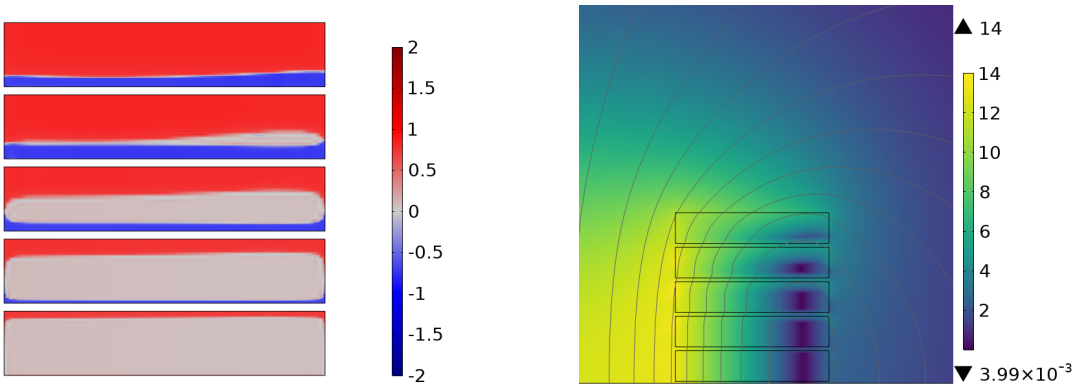

(a) (b)

Figure 3.28: (a) Normalized current density distribution during the steady-state phase (t = 650 s), showing current relaxation and creep leading to a more uniform current distribution and less screening currents compared to the peak time. (b) Corresponding magnetic field norm distribution.

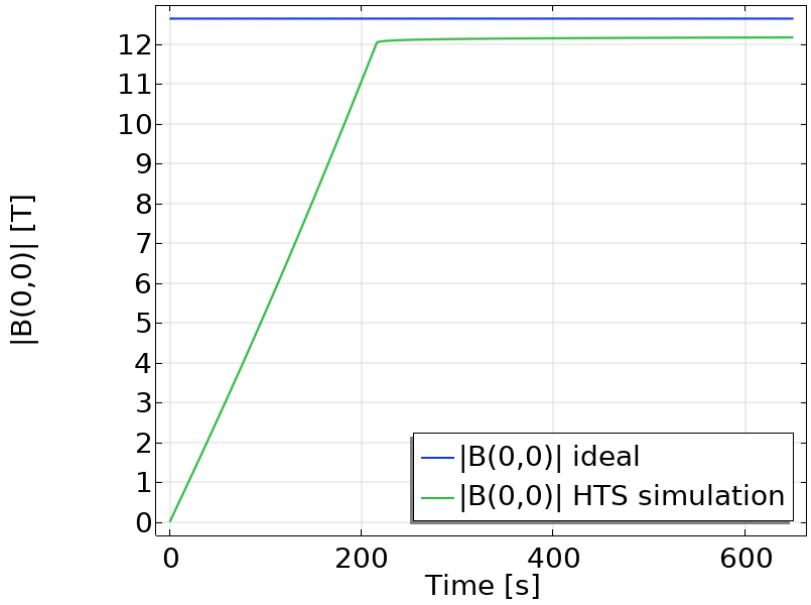

Figure 3.29: Time evolution of the magnetic field norm at the coil center ($|\mathbf{B}(0,0)|$), comparing the HTS simulation against the ideal uniform model, quantifying the large initial SCIF deficit ($B_{\text{SCIF}} \approx -0.57$ T) in the 10-pancake configuration.

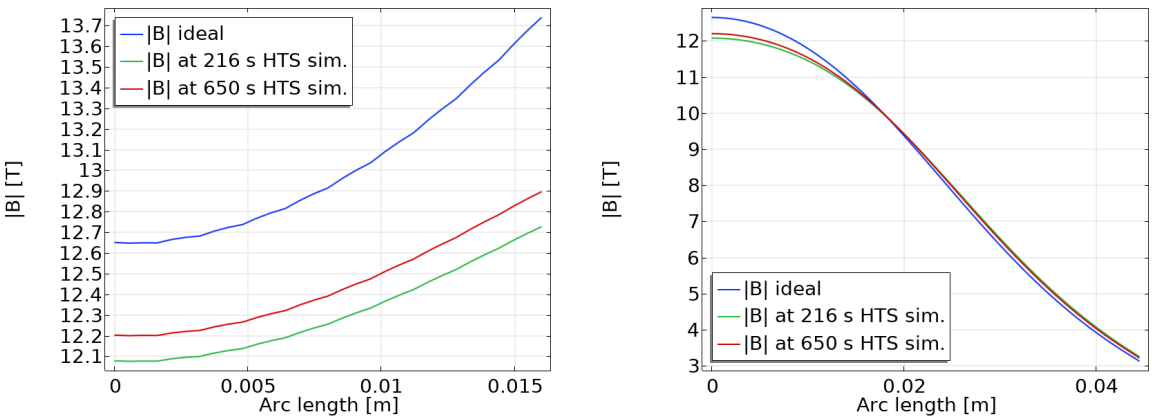

(a) Mid-plane line comparison

(b) Center-line comparison

Figure 3.30: Magnetic field norm profile along the (a) Mid-Plane Line and (b) Center Line of the 10-pancake coil, comparing the ideal case against the HTS simulation at peak time ($t = 216$ s) and steady state ($t = 650$ s).

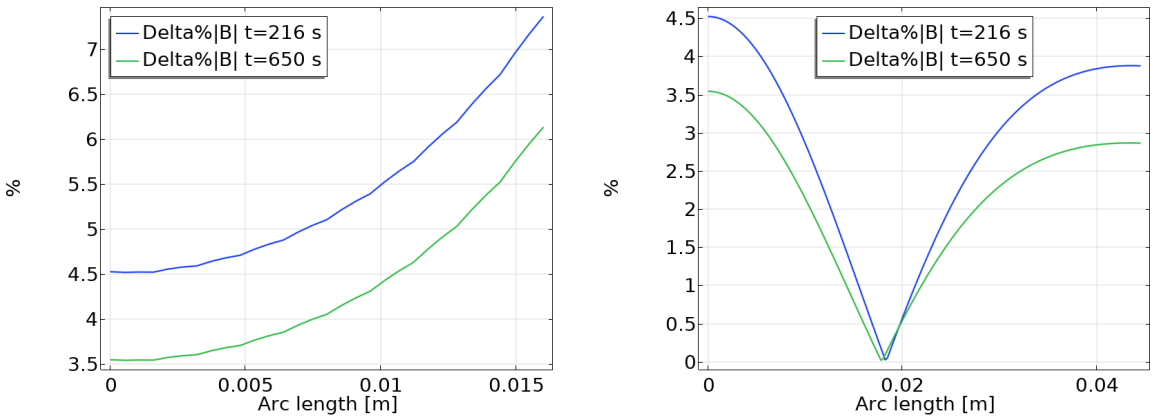

Figure 3.31: Relative percent difference (ϵ) in magnetic field norm ($|\mathbf{B}|$) between the HTS simulation and the ideal model ($\epsilon = \frac{|B_{\mathrm{HTS}} - B_{\mathrm{id}}|}{B_{\mathrm{id}}} \times 100$) along the center line (a) and the middle-plane (b), quantifying the progressive SCIF degradation

3.3.2.1 Central volume method

To investigate how the simulated magnetic field and the ideal magnetic field differ, a central volume is inserted. The dimension of the central volume follows the dimension of the mid-plane line arc length and the central line (respectively 80% of the inner radius and 150% of the half height).

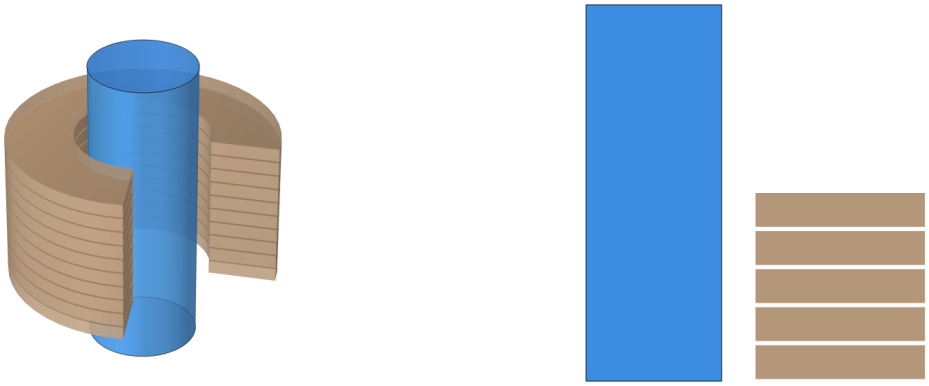

(a) (b)

Figure 3.32: Three-dimensional view of the pancake stack (a) and the corresponding 2D plane used to define the central volume for the evaluation of the field quality (b).

Figure 3.34 shows that the discrepancy between the ideal magnetic field magnitude and that obtained with the T–A formulation mainly arises from the axial component. To clarify the relative contributions of the two field components, Figure 3.35a presents an arrow plot where r-direction arrows represent the difference in the radial component, and z-direction arrows the difference in the axial component, between the HTS and uniform-current cases. The blue isoline identifies regions where the radial components coincide, while the red isoline marks those where the axial components are equal.

This visualization provides a clear spatial interpretation of how screening currents alter the local magnetic field distribution in HTS coils.

Following the $\Delta B_{r,z} = 0$ isolines (Fig. 3.35), the central volume can be divided into three regions:

- **Central Region:** the magnetic field produced by the uniform current distribution is higher in both the radial and axial directions (below the magenta line).
- **Upper Coils Region:** the magnetic field produced by the uniform distribution is higher only in the radial direction (between the black line and the magenta line).
- **Outside Coils Region:** the magnetic field produced by the uniform distribution is lower in both the radial and axial directions (above the black line).

It is evident that the main difference between B_{id} and B_{HTS} occurs in the mid-plane region (see fig. 3.33) and is primarily due to the axial component (3.34c). To further

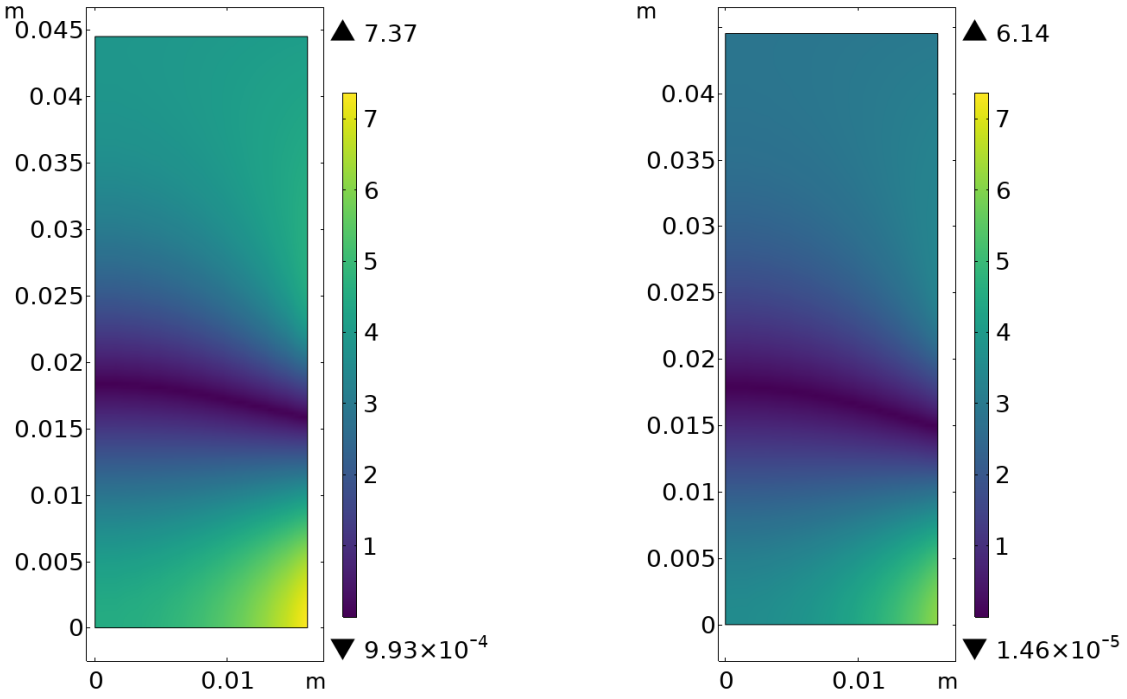

(a) t=216s (b) t=650s

Figure 3.33: Relative percentage difference field maps ($\epsilon = \frac{|B_{\text{HTS}} - B_{\text{ideal}}|}{|\mathbf{B}_{\text{ideal}}|}[\%]$) across the central volume at:(a) current peak (t = 216 s) and (b) steady state (t = 650 s)

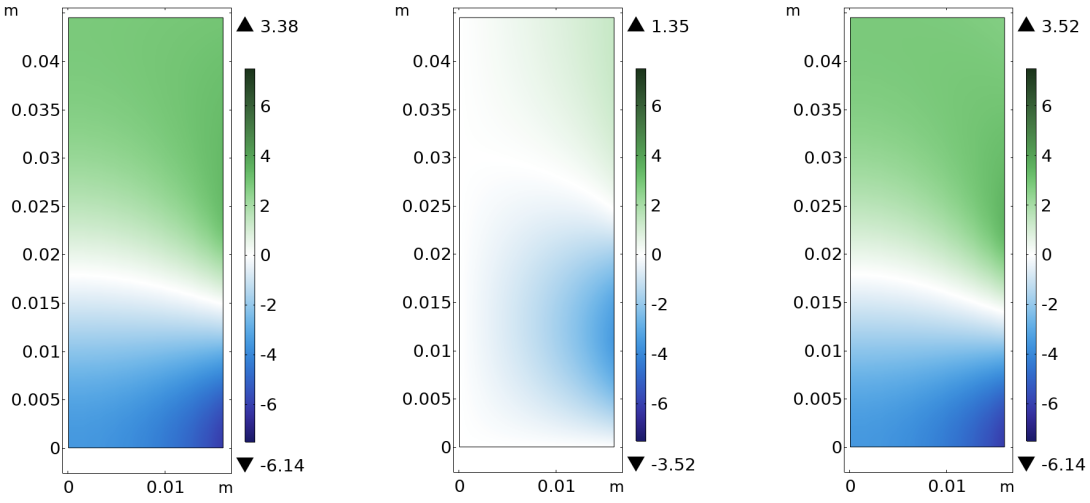

(a) $\frac{|B_{\text{HTS}}| - |B_{\text{ideal}}|}{|\mathbf{B}_{\text{ideal}}|}[\%]$ (b) $\frac{B_{\text{r,HTS}} - B_{\text{r,ideal}}}{|\mathbf{B}_{\text{ideal}}|}[\%]$ (c) $\frac{B_{\text{z,HTS}} - B_{\text{z,ideal}}}{|\mathbf{B}_{\text{ideal}}|}[\%]$

Figure 3.34: Relative percentage difference field maps ($\frac{B_{\text{HTS}} - B_{\text{ideal}}}{|\mathbf{B}_{\text{ideal}}|}[\%]$) across the central volume at steady state (t = 650 s): (a) Magnetic field magnitude $|\mathbf{B}|$, (b) Radial component B_r, and (c) Axial component B_z.

investigate the source of this discrepancy, it is useful to plot the axial component of the magnetic field for both type of models 4.2.

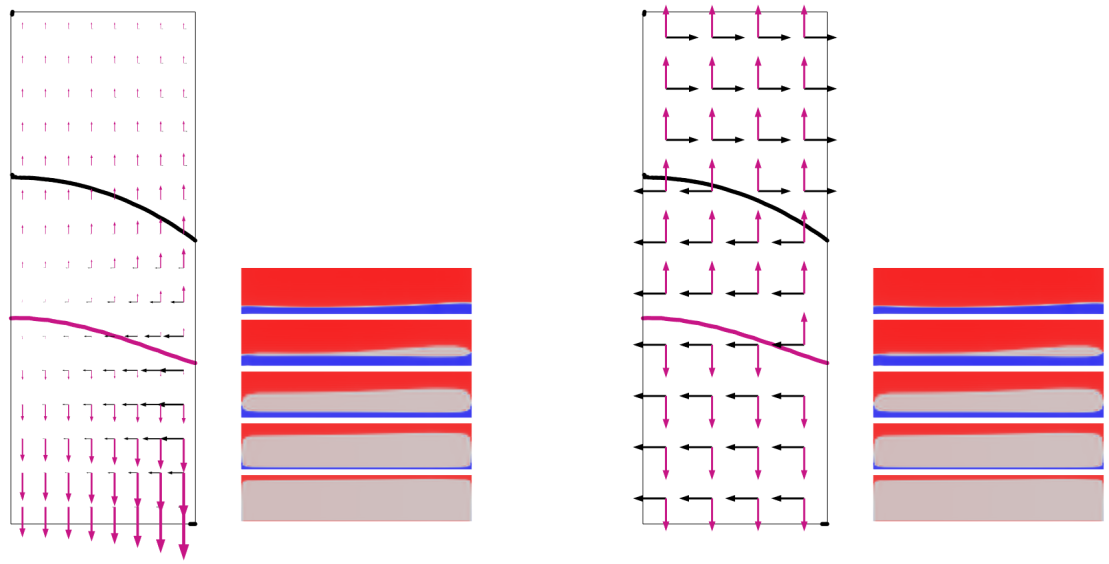

(a) (b)

Figure 3.35: Blue arrows $\propto B_{rHTS} - B_{rId}$; red arrows $\propto B_{zHTS} - B_{zId}$. Red line represent $B_{zHTS} - B_{zId} = 0$; blue line represent $B_{rHTS} - B_{rId} = 0$. In the right, the cross section of the pancake showing the current density distribution. In (b) normalized arrows.

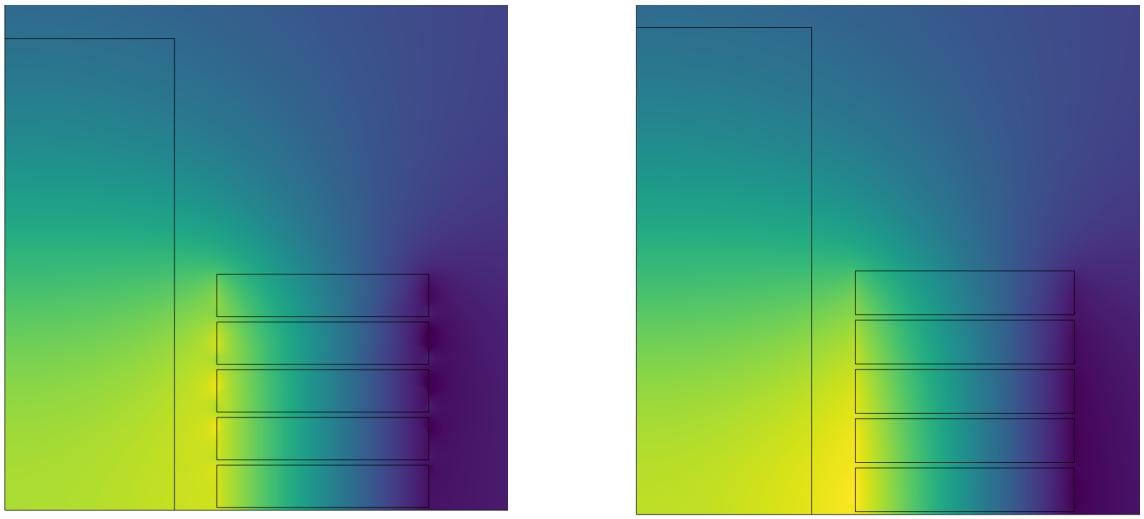

(a) B_z from HTS. (b) B_z from Uniform current distribution.

Figure 3.36: The pictures shows that the magnitude of B_z in the uniform current distribution (b) is higher in the center plane (brighter yellow) while in the HTS coils the B_z magnitude is more evenly distributed.

4 Magnetic Field Quality Optimization

The objective of this chapter is to identify strategies to improve the magnetic field quality of HTS pancake coil magnets. In this context, optimization refers to reducing the deviation between the magnetic field generated by the superconducting coil and the ideal magnetic field obtained by assuming a uniform current distribution.

The study was carried out in two stages.

In the first stage, a parametric analysis was performed to understand how variations in the main design and operating parameters—such as the maximum transport current, the number of pancakes, and the tape height—affect the electromagnetic behavior. In these preliminary investigations, the evaluation of magnetic field quality was always made by comparing the HTS results with the ideal magnetic field corresponding to the same configuration (i.e., accounting for the same geometry and current distribution). This approach ensured that any observed differences could be directly attributed to the intrinsic superconducting effects rather than to geometrical or electrical changes.

In the second stage, the insights gained from the parametric study and the analysis presented in the previous chapter were combined to propose a set of optimized configurations. These configurations aim to mitigate the effects of screening currents (SCIF) and to obtain a magnetic field distribution closer to the ideal one. Most of these optimized configurations were evaluated with respect to the default ideal field (B_{id}), although one configuration showed superior performance even when compared to the ideal field associated with its own current distribution ($B_{id,opt}$).

4.1 Parametric analysis and Sensitivity study

4.1.1 Increasing pancakes number

The first step of the optimization study consists in evaluating the influence of the number of pancakes on the magnetic field quality in the central region. In particular, two additional configurations are analyzed: a 16-pancake stack and a 20-pancake stack. To ensure consistency with the previous analyses, the input current is adjusted so as to maintain the magnetic field norm at the coil center at approximately 12.6 T. Consequently, a maximum current of 170 A is applied to the 16-pancake stack, while the 20-pancake stack reaches a peak current of 158 A. The results, presented in Fig. 4.1a and Fig. 4.1b, indicate that increasing the number of pancakes leads to a degradation of the magnetic field quality in both cases. This degradation can be attributed to the enhanced self-field effects and the stronger influence of screening currents in the outer pancakes, which distort the magnetic field distribution and reduce its uniformity in the central region.

(a) 16-Pancake Stack. (b) 20-Pancake Stack.

Figure 4.1: Three-dimensional representation of the extended HTS pancake coil geometries simulated for the parametric study: (a) 16-Pancake Stack and (b) 20-Pancake Stack.

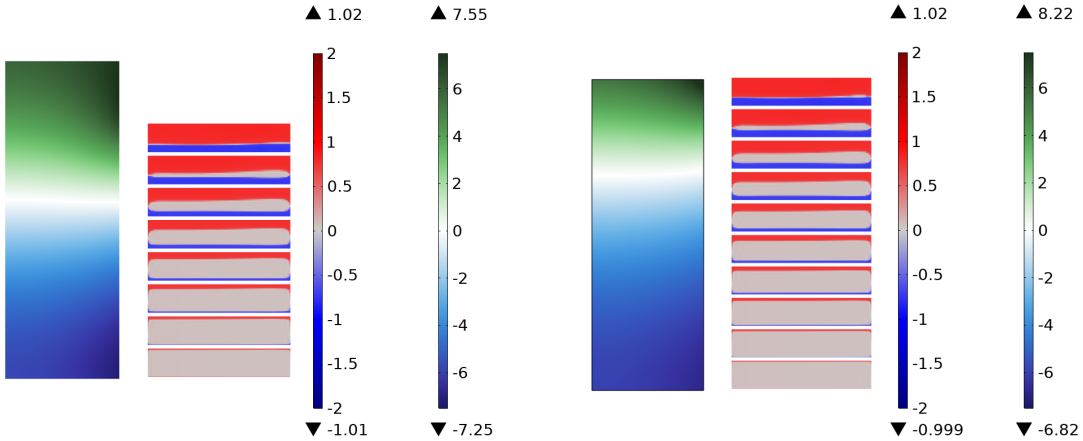

(a) 16-Pancake Stack. (b) 20-Pancake Stack.

Figure 4.2: Comparison of current density distribution ($J_\varphi / J_c(\vec{B})$) and magnetic field deviation ($\frac{B_{\mathrm{HTS}} - B_{\mathrm{id}}}{B_{\mathrm{id}}}$ [%]) in the central volume after increasing the number of pancakes.

4.1.2 Influence of the input current

In this section instead of consider only 70% of the maximum input current (I_c = 308 A) different value of maximum transport current (I_m) are considered:

- $I_m = 0.5Ic$ = 154 A;
- $I_m = 0.6I_c$ = 185 A;
- $I_m = 0.7I_c$ = 216 A;
- $I_m = 0.8I_c$ = 247 A;
- $I_m = 0.9I_c$ = 278 A.

The results indicate a clear improvement in the magnetic field quality as the input current increases (see Fig. 4.4). This phenomenon can be explained by the increased penetration of the transport current, as shown in Figure 4.5. Higher currents lead to a current density distribution that more closely resembles the ideal uniform distribution, thereby improving the magnetic field quality

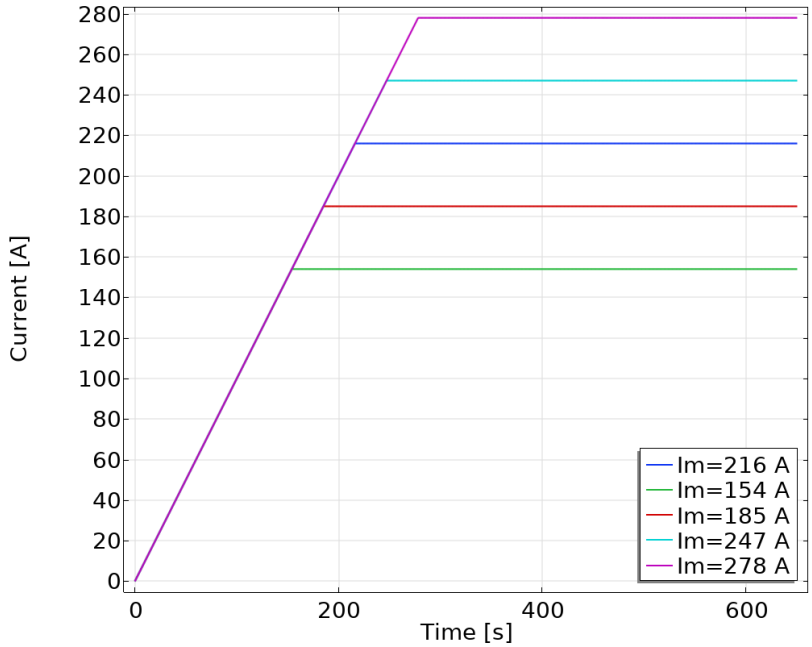

Figure 4.3: Input current profiles used for the sensitivity study on current magnitude, ranging from $I_m = 0.5I_c$ (154 A) to $I_m = 0.9I_c$ (278 A).

To better understand the reason why the magnetic field quality increase with the increasing of the current let's observe also the related current density distribution.

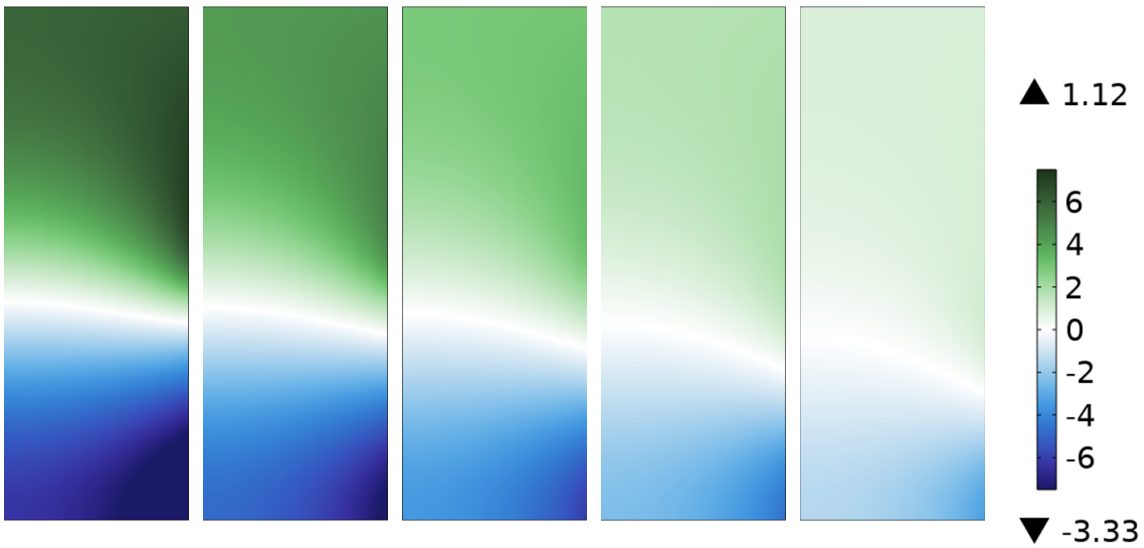

Figure 4.4: Evaluation of magnetic field quality ($\frac{B_{\mathrm{HTS}}-B_{\mathrm{id}}}{B_{\mathrm{id}}}[\%]$) within the central volume for different operating current levels (I_m), demonstrating improved homogeneity as the current penetration increases.

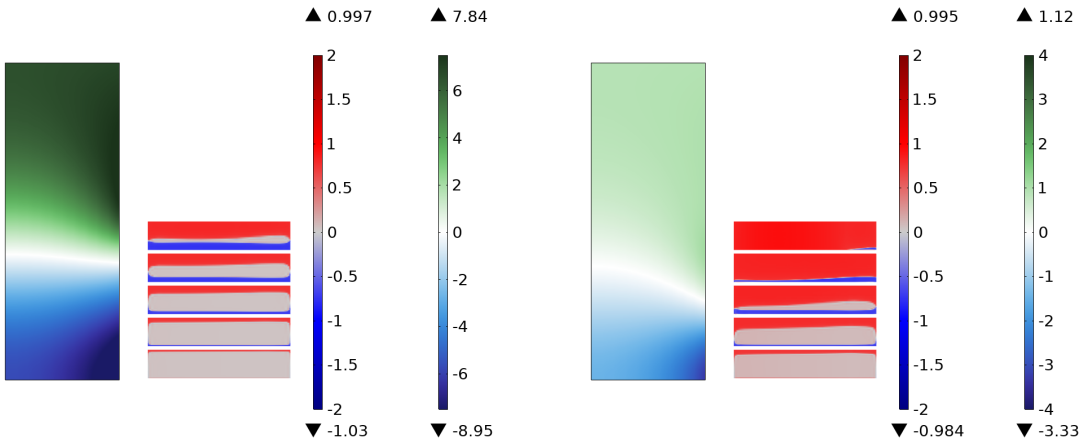

(a) $0.5Ic$ (b) $0.9Ic$

Figure 4.5: Comparative visualization of the current density distribution ($J_\varphi/J_c(\vec{B})$) and the corresponding field quality ($\frac{B_{\mathrm{HTS}}-B_{\mathrm{id}}}{B_{\mathrm{id}}}[\%]$) at $t = 650$ s for the lowest and highest operating points: (a) $I_m = 0.5I_c$ and (b) $I_m = 0.9I_c$.

4.1.3 Tape width influence

This section investigates the influence of tape width on the magnetic field quality. To this end, a simulation is performed using tapes with half the nominal width: instead of 4mm tapes, 2mm tapes are considered. The choice of 2mm is motivated by its commercial availability.

Reducing the tape width decreases the critical current per tape; to preserve the on-axis magnetic field intensity at the coil centre, the number of pancakes is therefore increased from 10 to 20 while the transport current per pancake is halved. In other words, by approximately maintaining the total ampere–turns of the stack, the central field magnitude remains comparable to the reference 10-pancake case, enabling a direct comparison of field quality between the two configurations. A similar simulation configuration (HTS tape striation) is reported in [2] and confirm the reduction of SCIF effect.

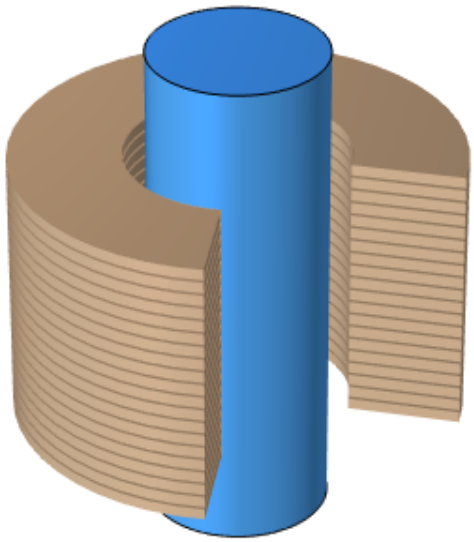

Figure 4.6: Three-dimensional representation of the optimized geometry utilizing tapes with reduced width (2 mm wide tapes in a 20-Pancake stack), preserving the total Ampere-turns.

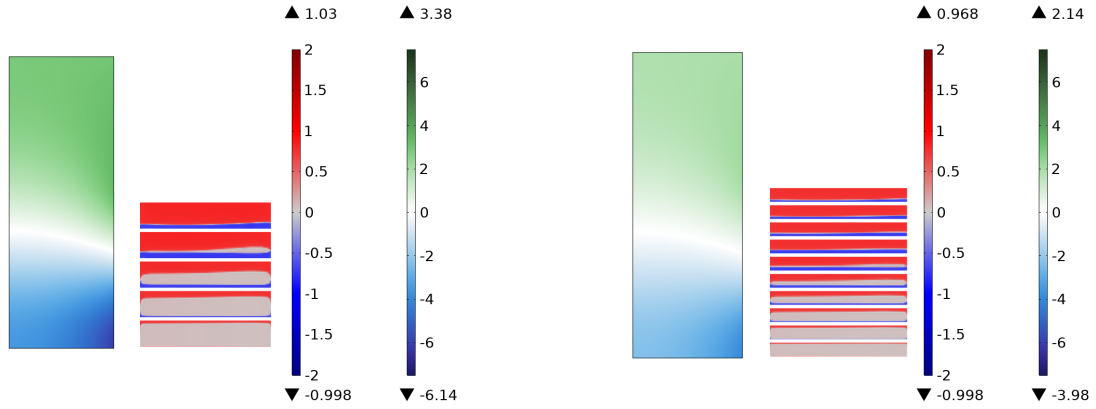

(a) (b)

Figure 4.7: Comparative analysis of field quality: (a) Reference 10-pancake stack with 4 mm tape width and (b) Optimized 20-pancake stack with 2 mm tape width and half input current (I_m = 154 A), illustrating the reduction of SCIF effects through geometric modification.

4.2 Optimized configurations

Based on the findings from the parametric studies and the analysis of screening currents in the standard 10-pancake coil, several configurations have been selected for further investigation. In this work, *optimization* is defined as modifications that improve the magnetic field uniformity in the central region by minimizing the deviation from a reference field. Depending on the case, the reference field may be either the ideal field of the standard 10-pancake coil (B_{id}) or the ideal field corresponding to the modified configuration itself ($B_{id,opt}$).

The configurations analyzed in this study are:

- Enhancement of the current in the central pancakes, with a reduction in the outer pancakes.
- Addition of an internal double-pancake coil.
- Reduction of the tape height by half in the central pancakes.
- Reduction of the tape height by half in the central double-pancake coil.

These cases are systematically studied to evaluate how variations in current distribution and tape geometry influence the magnetic field uniformity, providing insight into strategies for optimizing HTS pancake coil design.

4.2.1 Central-Current Enhancement with Reduced Current in Outer Pancakes

The optimization strategy is based on modifying the current distribution among the pancakes while preserving the target magnetic field at the coil center, i.e.

$$B_{\text{target}} = B_{\text{ref}}. \tag{4.1}$$

Where B_{target}, in this case, is the magnetic field generated by the reference configuration of 10-pancake stack with uniform current distribution. Let the coil be composed of N pancakes, each carrying a transport current I_i. In the reference configuration all pancakes carry the same current $I_i = I_0$. The magnetic field generated at the observation point is

$$B_{\text{ref}} = \sum_{i=1}^{N} B_i(I_0), \tag{4.2}$$

where $B_i(I)$ denotes the magnetic-field contribution of the i-th pancake when it carries a current I.

The optimization goal consists of finding a new set of currents

$$\mathbf{I} = \{I_1, I_2, \ldots, I_N\}$$

that satisfies the magnetic-field constraint

$$\sum_{i=1}^{N} B_i(I_i) = B_{\text{target}}, \tag{4.3}$$

while improving a chosen performance metric. Physically, a convenient solution is obtained by increasing the current in the central pancakes and decreasing it in the outer ones because the central pancakes contribute more efficiently to the on-axis magnetic field. This redistribution reduces the need for high current densities in regions where the local field is stronger and the critical current density is lower, thereby reducing losses. In the following simulation, the set of currents used are:

$$\mathbf{I} = \{I_1 = 7/8I_m, I_2 = 7/8I_m, I_3 = 7/8I_m, I_4 = 7/8I_m, I_5 = 3/2I_m\}$$

Here, I_m represents the maximum current (216 A) of the default configuration. I_1 designates the top pancake, and the coil's axial symmetry is preserved (i.e., I_5 is the central double pancake).

This adjustment yields a magnetic field spatial distribution that more closely matches the ideal reference field. Quantitatively, the relative error in the central volume is significantly reduced to approximately 1% (see Figure 4.9), representing a substantial improvement over the 3.5% to 6.14% error observed in the default configuration (Figure 3.31).

However, if the field quality evaluation metric were calculated against the ideal field corresponding to the new current distribution ($B_{\text{id,Opt}}$), there is no resulting reduction in relative error. This implies that while the optimized current set effectively compensates for the SCIF inherent to the HTS material compared to the uniform reference, the new, intentionally non-uniform current profile ($B_{\text{id,Opt}}$) inherently introduces slight deviations from perfect homogeneity when compared against its own ideal counterpart. Therefore, the success of this strategy is best measured by the reduction of the absolute deviation from the default uniform field reference.

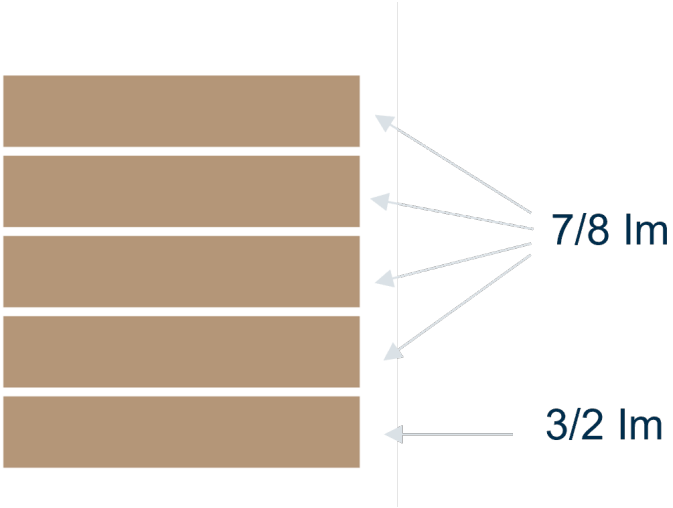

Figure 4.8: Schematic representation of the differential current distribution used for optimization: $I_{\text{outer}} = \frac{7}{8} I_m$ in pancakes 1-4 and $I_{\text{center}} = \frac{3}{2} I_m$ in the central pancake 5.

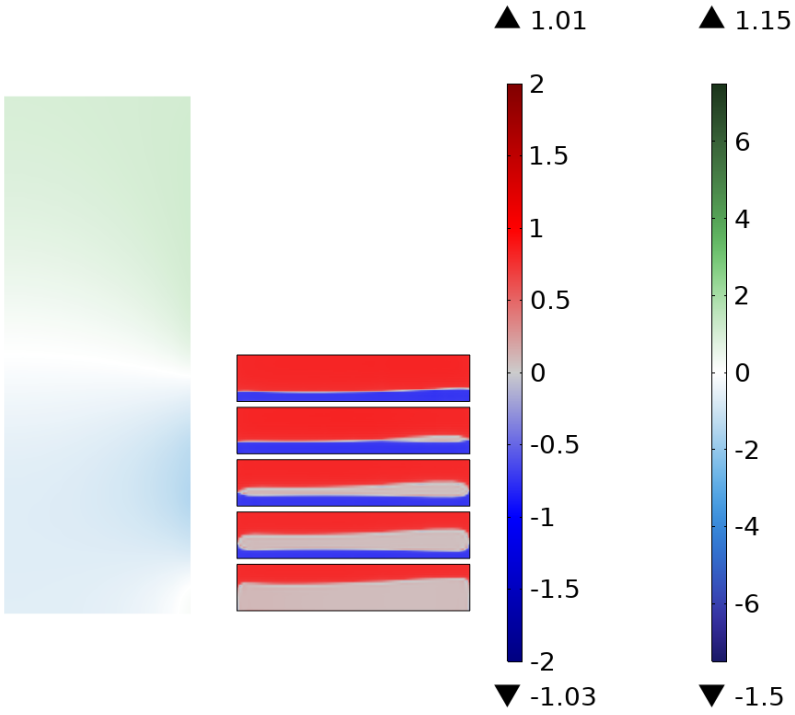

Figure 4.9: Comparison of the current distribution ($J_\varphi / J_c(\vec{B})$) and the magnetic field deviation ($\frac{B_{\text{HTS}} - B_{\text{id}}}{B_{\text{id}}}[\%]$) resulting from the differential current distribution.

4.2.2 Adding an internal double pancake coil

The second optimization strategy consists in inserting an additional double-pancake coil in the central bore of the stack. The internal coil is connected in series with the main pancakes and therefore carries the same transport current I. Its purpose is to generate a compensating magnetic field at the coil center that counteracts the Screening-Current-Induced Field (SCIF) produced by the HTS pancakes.

Analytical formulation. Denote by $B_{\mathrm{HTS}}(I)$ the axial field at the observation point (center) produced by the HTS pancake assembly (including the SCIF contribution), and by $B_{\mathrm{ref}}(I)$ the target (ideal) axial field produced by the same assembly assuming uniform current density. Let the internal double-pancake coil consist of N_{int} turns (total turns of the internal coil contributing to the axial field) and let b_{int} be the axial field per turn at the observation point when unit current flows (i.e. b_{int} depends only on geometry and the observation point). With the internal coil present and carrying current I, the total axial field becomes

$$B_{\mathrm{tot}}(I, N_{\mathrm{int}}) \;=\; B_{\mathrm{HTS}}(I) \;+\; N_{\mathrm{int}}\, b_{\mathrm{int}}\, I. \tag{4.4}$$

The compensation objective can be stated as finding an integer N_{int} such that the deviation from the ideal target field is minimized:

$$N_{\mathrm{int}}^{*} \;=\; \arg\min_{N_{\mathrm{int}}\in\mathbb{Z}^{+}} \left|B_{\mathrm{tot}}(I, N_{\mathrm{int}}) - B_{\mathrm{ref}}(I)\right|. \tag{4.5}$$

Using (4.4) this reduces to

$$N_{\mathrm{int}}^{*} \;=\; \arg\min_{N_{\mathrm{int}}\in\mathbb{Z}^{+}} \left|B_{\mathrm{HTS}}(I) - B_{\mathrm{ref}}(I) + N_{\mathrm{int}}\, b_{\mathrm{int}}\, I\right|. \tag{4.6}$$

If a continuous approximation is acceptable, the optimal (real) number of turns is

$$\tilde{N}_{\mathrm{int}} \;=\; -\,\frac{B_{\mathrm{HTS}}(I) - B_{\mathrm{ref}}(I)}{b_{\mathrm{int}}\, I}, \tag{4.7}$$

and the physically admissible integer solution is $N_{\mathrm{int}}^{*} = \mathrm{round}(\tilde{N}_{\mathrm{int}})$.

Applying the above procedure to the studied geometry and operating point (same current as the main pancakes) and using the computed values of B_{HTS}, B_{ref} and the geometric coupling b_{int}, the continuous estimate $\tilde{N}_{\mathrm{int}}$ yields a value close to 73.8. Because we are considering a Double pancake, each pancake needs to have a number of turns of 37.

$$N_{\mathrm{int}}^{*} \approx 37,$$

which was therefore adopted as the preliminary design for the internal double-pancake compensation coil. Time-dependent simulations including this internal coil are required to confirm the compensation efficacy and to check that no local over-critical regions are introduced during ramp and relaxation.

The internal double-pancake coil provides a direct, hardware-level way to counteract the SCIF at the magnet center. The method is straightforward: compute the compensating

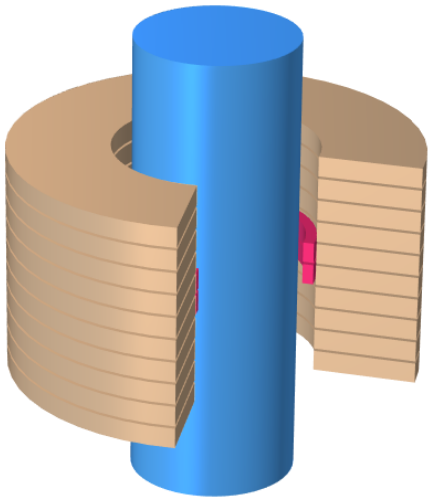

Figure 4.10: Three-dimensional representation of the compensation strategy: the main 10-pancake stack complemented by the optimized Internal Double Pancake Coil (IDPC) in the central bore.

field deficit at the operating current, evaluate the per-turn coupling of the internal coil geometry, and select the integer number of turns from equation (4.7).

The time-dependent simulations, including the optimized IDPC design, demonstrate its high effectiveness. As evident from Figure 4.11 , the resulting magnetic field profile, B_{HTS}, significantly reduces the deviation from the primary design specification B_{id}, achieving a relative error close to 0% in the central volume. This outcome confirms that adding a properly designed IDPC can offer a substantial contribution to the precise shaping of the magnetic field in relation to the default ideal field B_{id}.

As noted in Section 4.2, it is crucial to clarify the reference choice:

The success of this strategy is measured by the error calculated with respect to the original design goal:$(B_{\mathrm{HTS}} - B_{\mathrm{id}})/B_{\mathrm{id}}$. However, if the field quality evaluation were performed using the ideal field generated by this optimized configuration ($B_{\mathrm{id,opt}}$) as the reference, the results show a negligible improvement in the relative error.This confirms that the IDPC strategy is primarily an active mitigation of the persistent SCIF effects, successfully forcing the HTS magnet's performance (B_{HTS}) to match the required uniform design target (B_{id}).

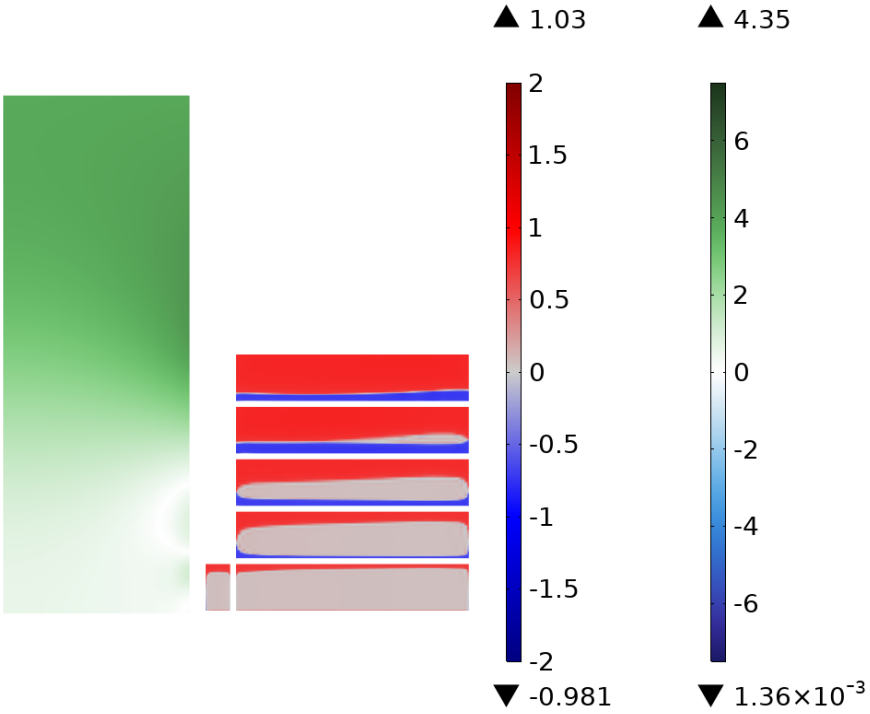

Figure 4.11: Field quality evaluation for the IDPC compensated configuration, demonstrating the substantial reduction of the relative error ($\frac{B_{\mathrm{HTS}}-B_{\mathrm{id}}}{B_{\mathrm{id}}}$ [%]) towards 0% in the central volume.

4.2.3 Reduction of Tape Height in the Central Double Pancakes

In this configuration, the height of the two central double pancakes is reduced while keeping the transport current in each pancake unchanged. Although the geometric cross-section of the central pancakes decreases, this does not require a reduction of the applied current. The reason is that, in the central region of the stack, the current density distribution strongly limits magnetic-field penetration. As a consequence, the local critical current density increases, allowing the smaller tapes to carry the same transport current without violating the superconducting constraint.

This geometric modification aims at reducing the screening-current contribution in the innermost region of the coil, thus improving the overall magnetic field quality without altering the global operating conditions of the magnet.

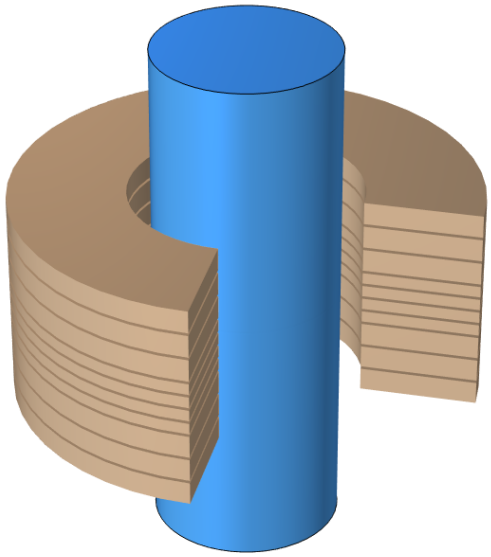

Figure 4.12: Three-dimensional view of the geometry with the tape height reduced in the two central double pancakes.

The simulation results, illustrated in Figure 4.13, confirm the effectiveness of this approach: the current density distribution becomes more uniform in the center, mitigating the localized effects of the screening currents. The magnetic field quality evaluation, calculated as the relative error with respect to the ideal field generated by this specific geometric configuration ($B_{\mathrm{id,opt}}$), is presented for the center volume in the figure.

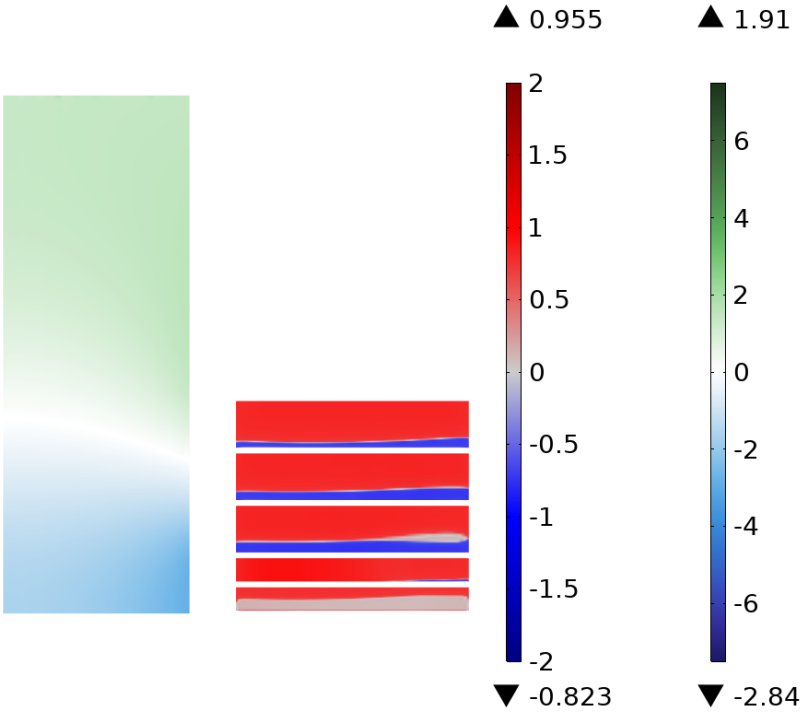

Figure 4.13: Current density distribution ($J_\varphi / J_c(\vec{B})$) and magnetic field deviation ($\frac{B_{\mathrm{HTS}} - B_{\mathrm{id,opt}}}{B_{\mathrm{id,opt}}}$ [%]) for the two-CDPC reduced height configuration, confirming the more uniform current distribution in the center.

4.2.4 Reduction of the tape height by half in the central double-pancake coil

This configuration is geometrically similar to the previous strategy (Section 4.2.3), but here we focus the geometric modification on only one central double pancake coil instead of two. The methodology of maintaining the transport current I unchanged is applied, utilizing the enhanced local critical current density $J_c(\mathbf{B})$ in the central region of the stack.The results confirm the efficacy of this precise geometric modification. The simulated field B_{HTS} demonstrates a significant increase in magnetic field quality when compared to the baseline 10x4mm default configuration (B_{id}).

Crucially, the evaluation of the resulting field quality shows a minor, yet observable, improvement with respect to both reference metrics:

- Improvement vs. B_{id} (Design Target): This confirms the substantial mitigation of SCIF, making this configuration a viable candidate for achieving the original design specification (4.15(a)).
- Improvement vs. $B_{\mathrm{id,opt}}$ (Specific Geometric Reference): This result provides key physical validation. The reduction of the residual error $(B_{\mathrm{HTS}} - B_{\mathrm{id,opt}})/B_{\mathrm{id,opt}}$ confirms that decreasing the volume susceptible to SCIF generation in the high-J_c region (the center) is an effective geometric tool for maximizing uniformity inherent to the modified design (4.15(b)).

The overall contribution of this study is significant, confirming the superiority of this design over the default 10x4mm-pancake stack.

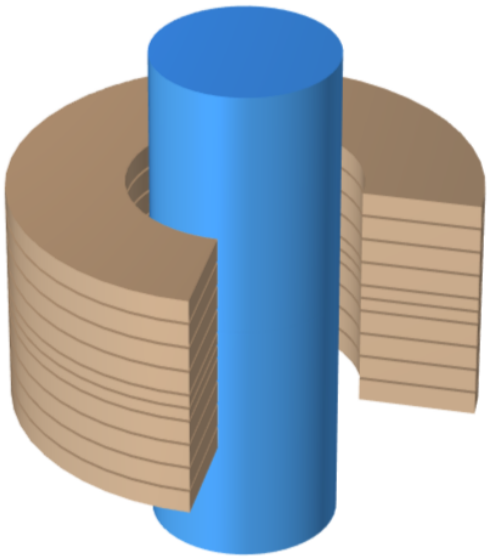

Figure 4.14: Three-dimensional view of the geometry with the tape height reduced only in the single central double pancake.

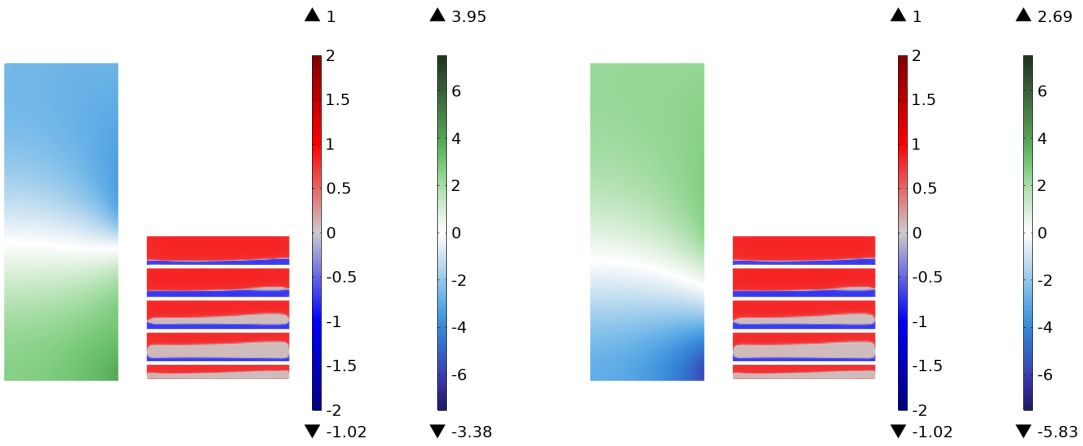

(a) (b)

Figure 4.15: Comparative visualization of field quality: (a) Reference 10-pancake stack (4 mm width) vs (b) Single-CDPC Reduced Height configuration, illustrating the slight improvement observed against both B_{id} and $B_{\mathrm{id,opt}}$.

5 Conclusion

The master's thesis project focused on providing a rigorous electromagnetic characterization of Screening Current Induced Fields (SCIF) in HTS electromagnets and assessing their impact on overall field performance. This work developed and applied numerical simulation tools, essential for the optimal design of superconducting magnets requiring high and homogeneous magnetic fields.

The adoption of the Homogenized T–A Formulation was critical throughout the study. This formulation enabled the execution of numerous robust simulations and parametric studies, facilitating a systematic progression towards highly relevant configurations and results.

The primary findings derived from the analysis are summarized as follows:

1. **Degradation of Transportable Current and Geometric Dependence.** The geometric configuration of the HTS stack significantly influences the achievable Maximum Transport Current ($I_{\max}$). Utilizing the I–E criterion and the Load Line Method, a quantified reduction in the current capacity ($I_{\max}$) while maintaining the superconducting state was established. Specifically, the maximum transport current capacity, relative to the zero-field critical current (I_{c0}), drastically decreases with stack height due to self-field effects: $\approx$ 26.4% for a single pancake, $\approx$ 17.2% for a four-pancake stack, and $\approx$ 14% for the ten-pancake configuration. These results underscore the magnetic interaction between pancakes as the primary operational constraint (Results detailed in Table 5.1.)

2. **SCIF Impact and Field Quality Deterioration.** The number of pancakes in a series-connected HTS stack critically affects the magnet's electromagnetic behavior. As the number of pancakes increases, a progressive rise in the detrimental impact of SCIF was observed. This effect results in a deterioration of the Field Quality measured against the ideal uniform current design field (B_{id}). For the 10-pancake configuration, SCIF caused a field deviation in the central volume between -6.14% and 3.5% relative to B_{id}, confirming the necessity for effective mitigation strategies.

3. **Efficacy of SCIF Mitigation Strategies**. It was demonstrated that effective strategies for mitigating field non-uniformity can be achieved by manipulating both the coil geometry and the current distribution. Among the strategies studied, those yielding the most significant results include:

    - Current Redistribution: Increasing the current in the central coils while reducing it in the outer coils successfully forced a more uniform effective current density, reducing the primary field error to approximately 1% relative to B_{id}.

- Geometric Optimization (Reduced Tape Height): Decreasing the tape height in the central region represented a robust geometric approach. This configuration was unique in demonstrating a positive improvement in Field Quality against both the design target (B_{id}) and its own ideal geometric reference ($B_{\text{id,opt}}$), validating the physical principle that reducing the HTS volume in high-J_c regions is effective for residual SCIF suppression (Results detailed in Table 5.1).

Configuration	$I_{\max}[A]$	$I_{\max}/I_{c0}$ [%]
1-Pancake	580	26.4%
4-Pancake	378	17.2%
10-Pancake	308	14.0%

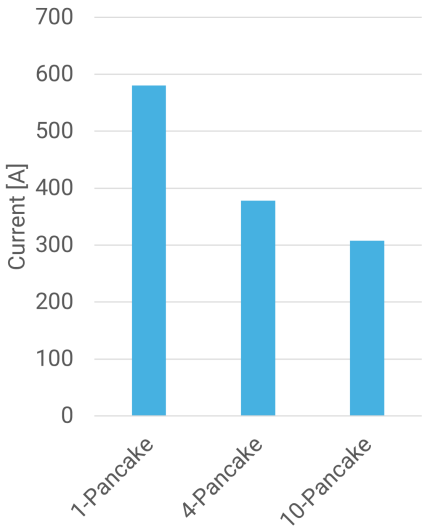

Figure 5.1: Degradation of Maximum Transport Current ($I_{\max}$) Across HTS Pancake Stacks

Configuration	$B_{\text{HTS}}(0,0) - B_{\text{id}}(0,0)[T]$	$B_{\text{HTS}}(0,0) - B_{\text{id,opt}}(0,0)[T]$
Baseline (10-Pancake)	−0.57	−0.57
Current Redistribution	−0.08	−0.50
IDPC Compensated	0.007	−0.44
Reduced t_c in 2DPC	0.33	−0.22
Reduced t_c in 1DPC	1.1	−0.1

Table 5.1: Summary of Absolute Magnetic Field Deviation at the Center Point ($B_{HTS} - B_{ref}$), demonstrating SCIF mitigation success against the original design target ($\mathbf{B}_{\text{id}}$) and the Intrinsic SCIF level of the configuration itself ($\mathbf{B}_{\text{id,opt}}$).

Model Limitations and Future Development While the current electromagnetic model successfully provided the critical insights needed for effective SCIF mitigation and $\mathbf{I}_{\max}$ prediction, the analysis operates within the constraints of a 2D axisymmetric domain and a single-physics framework. The subsequent and indispensable step for transitioning this research toward engineering design requires model extension in two critical directions. Firstly, a full three-dimensional (3D) model extension is paramount. The current simplification cannot capture the complex field profiles and stability margins inherent to

non-axisymmetric fusion magnets, such as the Stellarator coils central to our collaborative context. Secondly, robust multi-physics integration is essential, with a primary focus on thermomechanics . HTS magnets generate immense Lorentz forces; therefore, the model must couple the electromagnetic solution ($\mathbf{F} = \mathbf{J} \times \mathbf{B}$) with computational mechanics to calculate stress and strain (σ, ε). This integration is non-negotiable, as mechanical strain directly influences the local critical current density ($J_c(\varepsilon)$). Ultimately, coupling these domains is vital for validating structural integrity and accurately predicting quench initiation, thereby developing a reliable engineering tool for the complete operational lifecycle of HTS fusion magnets.

Bibliography

[1] Edgar Berrospe-Juarez et al. “Real-time simulation of large-scale HTS systems: multi-scale and homogeneous models using the T–A formulation”. In: *Superconductor Science and Technology* 32.6 (Apr. 2019), p. 065003. DOI: 10.1088/1361-6668/ab0d66. URL: https://doi.org/10.1088/1361-6668/ab0d66.

[2] Edgar Berrospe-Juarez et al. “Screening Current-Induced Field and Field Drift Study in HTS coils using T-A homogenous model”. In: *arXiv preprint arXiv:1908.06330* (2019). URL: https://arxiv.org/abs/1908.06330.

[3] Pablo Cayado. “Preparation of GdBa2Cu3O7 superconducting films by chemical solution deposition”. MA thesis. Università di Barcellona, 2012. DOI: 10.13140/RG.2.2.31893.88808.

[4] A. J. Creely et al. “Overview of the SPARC tokamak”. In: *Journal of Plasma Physics* 86.5 (2020), p. 865860502. DOI: 10.1017/S0022377820001257.

[5] Dirk van Delft. “History and significance of the discovery of superconductivity by Kamerlingh Onnes in 1911”. In: *Physica C: Superconductivity* 479 (2012). Proceedings of VORTEX VII Conference, pp. 30–35. ISSN: 0921-4534. DOI: https://doi.org/10.1016/j.physc.2012.02.046. URL: https://www.sciencedirect.com/science/article/pii/S0921453412000962.

[6] Jeffrey P. Freidberg. *Plasma Physics and Fusion Energy*. Cambridge University Press, 2007.

[7] Kyoto Fusioneering. *News: 3145*. Accessed: 20 October 2025. May 2025. URL: https://kyotofusioneering.com/en/news/2025/05/28/3145.

[8] Philippe Mangin and Rémi Kahn. *Superconductivity: An Introduction*. 1st ed. Physics and Astronomy eBook Package. Copyright © Springer International Publishing AG 2017. Cham: Springer International Publishing, 2017, pp. XVI + 379. ISBN: 978-3-319-50527-5. DOI: 10.1007/978-3-319-50527-5. URL: https://doi.org/10.1007/978-3-319-50527-5.

[9] Teruo Matsushita. “Measurement Methods for Critical Current Density”. In: *Flux Pinning in Superconductors*. Berlin, Heidelberg: Springer Berlin Heidelberg, 2007, pp. 209–231. ISBN: 978-3-540-44515-9. DOI: 10.1007/978-3-540-44515-9_5. URL: https://doi.org/10.1007/978-3-540-44515-9_5.

[10] Laheeb Mohammed and Kareem Jasim. “Study and compare influence of the partial substitution of copper nickel on the physical properties of superconducting compounds”. PhD thesis. University of Baghdad, Nov. 2018.

[11] Pia Jensen Ray. *Figure 2.4 in Master's thesis, "Structural investigation of La2–xSrxCuO4+y - Following staging as a function of temperature"*. Master's thesis, Niels Bohr Institute, Faculty of Science, University of Copenhagen. Accessed via Figshare. Copenhagen, Denmark, Nov. 2015. DOI: 10.6084/m9.figshare.2075680.v2.

[12] Karl Tischler and Alberto Leggieri. *Gyrotrons: The Backbone of Fusion Energy*. Accessed: 2025-09-08. Oct. 2024. URL: https://euro-fusion.org/eurofusion-news/gyrotrons-the-backbone-of-fusion-energy/.

[13] Huiming Zhang, Min Zhang, and Weijia Yuan. "An efficient 3D finite element method model based on the T–A formulation for superconducting coated conductors". In: *Superconductor Science and Technology* 30.2 (Dec. 2016), p. 024005. DOI: 10.1088/1361-6668/30/2/024005. URL: https://doi.org/10.1088/1361-6668/30/2/024005.

[14] X. Zhang et al. "General approach for the determination of the magneto-angular dependence of the critical current of YBCO coated conductors". In: *Superconductor Science and Technology* 30.2 (2017), p. 025010. DOI: 10.1088/1361-6668/30/2/025010. URL: https://doi.org/10.1088/1361-6668/30/2/025010.